

Autophagy inhibitor sensitized artificial activated neutrophil against hepatocellular carcinoma

Caixia Yang^{1, 2, 3, 4, 5#}, Huang Yang^{1, 6#}, Zhengwei Mao^{1, 6*}, Weilin Wang^{1, 2, 3, 4, 5*}, Yuan Ding^{1, 2, 3, 4, 5*}

¹ Department of Hepatobiliary and Pancreatic Surgery, the Second Affiliated Hospital, Zhejiang University School of Medicine, Hangzhou, Zhejiang 310009, China

² Key Laboratory of Precision Diagnosis and Treatment for Hepatobiliary and Pancreatic Tumor of Zhejiang Province, Hangzhou, Zhejiang 310009, China

³ Research Center of Diagnosis and Treatment Technology for Hepatocellular Carcinoma of Zhejiang Province, Hangzhou, Zhejiang 310009, China

⁴ National Innovation Center for Fundamental Research on Cancer Medicine, Hangzhou, Zhejiang 310009, China

⁵ Cancer Center, Zhejiang University, Hangzhou, Zhejiang 310058, China

⁶ MOE Key Laboratory of Macromolecular Synthesis and Functionalization, Department of Polymer Science and Engineering, Zhejiang University, Hangzhou, Zhejiang, China

Contributed equally.

* Corresponding author.

E-mail address: dingyuan@zju.edu.cn (Yuan Ding); wam@zju.edu.cn (Weilin Wang);

zwmao@zju.edu.cn (Zhengwei Mao)

Telephone and fax numbers: Tel: +86057187783820; Fax: +86057187068001

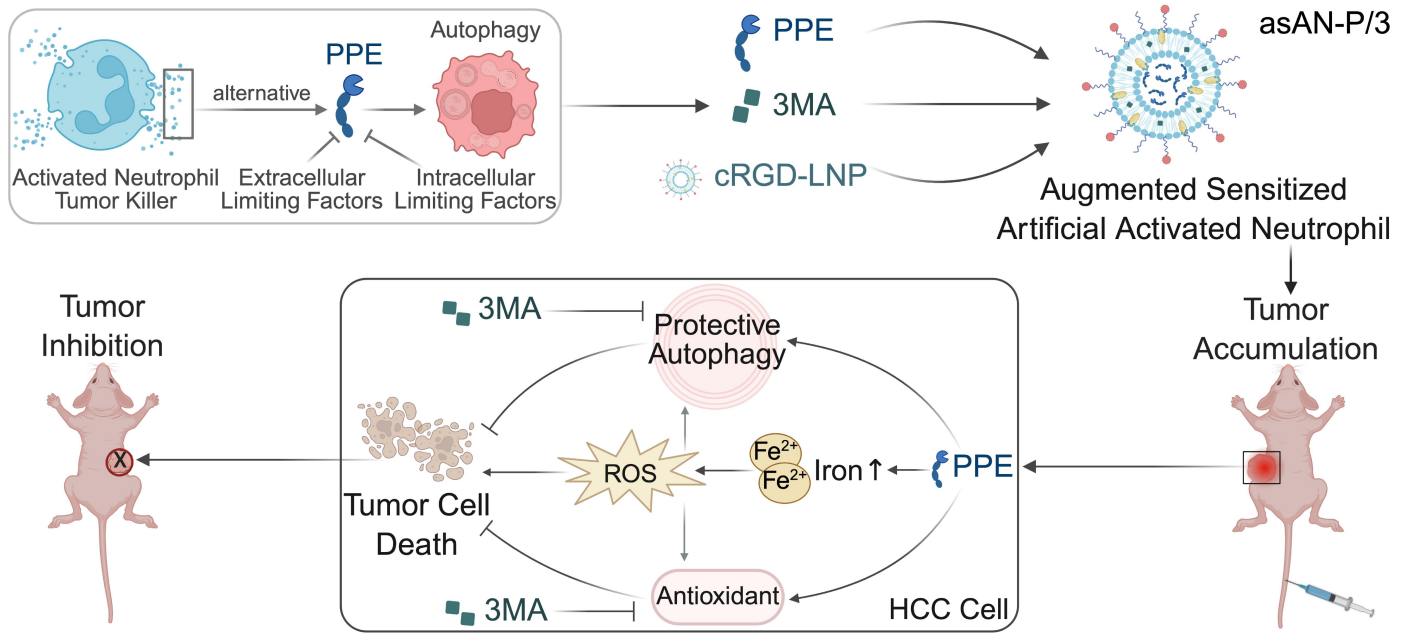
OCIRD: 0000-0001-9432-2649 (Weilin Wang).

Abstract

Activated neutrophils has emerged as a promising anti-neoplastic method in oncology. However, challenges including short lifespan, tumor microenvironment susceptibility, and pro-tumorigenic risks limited their clinical application. While artificial neutrophils addressed some limitations, few tumor-related studies were conducted, with constraining factors including specific targeting inefficiency, immunogenicity and manufacturing challenges. Neutrophil elastase (ELANE), a key antitumor effector in activated neutrophils, was functionally mimicked by porcine pancreatic elastase (PPE), which exhibited selective cancer cytotoxicity. However, PPE triggered protective autophagy in hepatocellular carcinoma (HCC), limiting therapeutic effectiveness. **Methods:** to overcome this resistance, we sensitized PPE by the autophagy inhibitor 3-methyladenine (3MA), co-delivered via tumor-targeting liposome, protecting drugs and improving the therapeutic efficacy both *in vitro* and *in vivo*. **Results:** 3MA enhanced iron-related ROS-mediated cell destruction induced by PPE while suppressing pro-survival autophagy. The augmented sensitized artificial activated neutrophil (asAN-P/3) showed precise tumor targeting, excellent therapeutic efficacy, prolonged survival and favorable bio-compatibility. **Conclusions:** we established a precise neutrophil-related tumor therapeutic method (asAN-P/3) and elucidated the mechanistic insights into PPE-mediated therapeutic limitations in HCC. Our study provided a substantial framework for neutrophil-derived anti-tumor therapeutic strategies in oncology.

Key words: Artificial activated neutrophil; Autophagy; Sensitization; Iron; HCC

48 **Graphic abstract**



65 **Introduction**

66 Hepatocellular carcinoma (HCC), the sixth most common malignancy and third-leading cause of
67 cancer mortality globally. Established risk factors included virus infections [1], non-alcoholic fatty liver
68 disease, alcohol-associated cirrhosis and iron overload [2]. For early-stage HCC, a significant proportion
69 of patients about 30-50% experienced tumor recurrence within 3 years [3]. For advanced stages,
70 sub-optimal drug efficacy and adverse effect constrained the efficacy [4]. Therefore, further research is
71 imperative to develop novel and effective treatment modalities for HCC.

72 Activated neutrophils have emerged as promising anti-neoplastic agents due to their specific
73 anti-tumor ability [5]. However, neutrophil related therapy was in high demand of cells from the patient
74 themselves, which may cause side effects [6]. Moreover, their clinical translation was hindered by
75 pro-tumorigenic plasticity [5], short lifespan, logistical challenges in cell sourcing and resistance to
76 genome editing also restricted their application [7,8].

77 Artificial neutrophils related research currently focused primarily on inflammatory treatments, with
78 less attention given to the application in oncology [9]. Research in oncology primarily utilized
79 neutrophil membranes, whereas immune cell membranes were mainly derived from the immortalized
80 cells, which may lead to undesirable biological effects. Furthermore, the targeting ability of neutrophil
81 membranes depended on the level of inflammatory chemotaxis signaling in the tumor [6]. Additionally,
82 membrane immunogenicity, immune response to denatured proteins produced during preparation, the
83 integrity of membrane proteins, and the costs of production all constrained their application [10].

84 Therefore, there is a need for more efficient, stable, specific, safe and cost-controllable methods for
85 artificial neutrophil related anti-tumor therapy.

86 Recent studies have demonstrated that activated neutrophils exerted anti-tumor effect primarily
87 through neutrophil elastase (ELANE). It internalized into tumor cells and selectively induced apoptosis
88 of tumor cells [11,12]. Porcine pancreatic elastase (PPE), a promising cost-effective alternative of
89 ELANE [11,13], could be constrained by the natural protease inhibitors in the blood [14,15],
90 extracellular connective tissue [16], non-targeted distribution and availability of the receptors [17-19].

91 Therefore, we attempted to utilize a bio-compatible liposome to create an artificial activated

neutrophil to protect it [20]. Considering the limited targeting ability of liposomes, we integrated the tumor-homing cyclic RGD (cRGD) peptide as a critical component to guide the chemotaxis of artificial activated neutrophils to tumor tissues. It could specifically bind to the $\alpha v\beta 3$ integrin overexpressed in tumor cells [21], conferring upon the artificial activated neutrophil a more stable targeting ability. Moreover, it was facile to synthesize and had broader applicability, thereby facilitating clinical translation.

Critically, we identified a limitation in PPE mediated therapeutic against HCC, attributed to the activation of autophagy. Autophagy, as a pro-survival mechanism in cancer cells, was associated with resistance of cancer therapies, protecting tumor from death [22].

Therefore, it is worthwhile to consider enhancing the effectiveness of PPE by inhibiting autophagy. 3-Methyladenine (3MA) was a classical early-stage autophagy inhibitor that targeted phospholipase-like III enzymes (PI3K). It has shown broad applicability in tumor treatments with a favorable safety profile [23,24]. Subsequently, we incorporated 3-MA to sensitize the artificial activated neutrophil. Consequently, we developed an augmented sensitized artificial activated neutrophil with excellent targeting capability for HCC therapy.

In this work, we discovered a limited therapeutic efficacy of the key activated neutrophil killing effector mimicker (PPE) in HCC, with the characteristic of activated protective autophagy. Therefore, 3MA was employed to sensitize the efficacy of PPE. The combination therapy disrupted iron-related ROS homeostasis and autophagy-mediated survival, synergistically enhancing apoptosis. Subsequently, we developed an augmented sensitized artificial activated neutrophil asAN-P/3 for HCC therapy (**Scheme 1**). It exhibited robust anti-tumor efficacy and prolonged survival *in vitro* and *in vivo*, with precise tumor targeting and bio-compatibility. As a consequence, this work contributed valuable insights for the advancement of the emerging neutrophil-related therapeutics in oncology.

Experimental Methods

Materials

118 All reagents and solvents were obtained commercially and utilized without subsequent purification.
119 Phosphate buffer solution (PBS), DMEM, fetal bovine serum and penicillin-streptomycin (100X) were
120 purchased from Gibco (USA). 3-Methyladenine (3MA), N-Acetylcysteine (NAC), Cell Counting Kit-8
121 (CCK8) and tetramethylrhodamine ethyl ester (TMRE) were purchased from MCE (China). Porcine
122 pancreatic elastase (PPE) was purchased from Worthington (USA). Chloroquine (CQ), deferoxamine
123 (DFO) and N-Methoxysuccinyl-Ala-Ala-Pro-Val p-nitroanilide (elastase substrate) were purchased from
124 Sigma-Aldrich (USA). Cholesterol was purchased from Aladdin (China). DSPE-PEG2000 was
125 purchased from Ruixibio (China). Lecithin was purchased from Yuanye Bio Technology (China). Cyclo
126 (RGD-Gly-C16) (c-RGD) was purchased from Nanjing Yuanpeptide Biotechnology Co., Ltd.
127 (Nanjing ,Jiangsu). Anti-Nrf2 (Cat# ab62352), anti-CD71 (Cat# ab214039), anti-Ferritin (Cat# ab75973),
128 anti-IRS1 (Cat# ab40777), anti-LC3B (Cat# ab192890), anti-Ki67 Cat# (ab15580) and anti-DMT1 (Cat#
129 ab55735) antibodies were purchased from Abcam (UK). Anti-ATG7 (Cat# 8558S), anti-ATG5 (Cat#
130 12994S), anti-cleaved caspase 3 (Asp175) (Cat# 9661T), anti-p62 (Cat# 88588S), anti-HIF1 α (Cat#
131 14179s) and anti-s-XBP1 (Cat# 40435s) antibodies were purchased from Cell Signaling Technology
132 (USA). Anti- β actin (Cat# 20536-1-AP) and anti-GAPDH (Cat# 60004-1-Ig) were purchased from
133 Proteintech (USA). Anti-tubulin (Cat# A12289) was purchased from Abclonal (China). LDH
134 Cytotoxicity Assay Kit, BeyoClick™ EdU Cell Proliferation Kit with Alexa Fluor 488,
135 Ad-mCherry-GFP-LC3B and One Step TUNEL Apoptosis Assay Kit were purchased from Beyotime
136 (China). Calcein-AM/PI live/dead cell staining kit was purchased from Solarbio (China). Cell cycle
137 staining Kit was purchased from MULTI SCIENCES (China). CM-H2DCFDA (DCFH), Hoechst 33342
138 and DAPI were purchased from Thermo Fisher Scientific (USA). FerroOrange, Annexin V FITC
139 Apoptosis Detection Kit, SOD Assay Kit and GSSG/GSH Quantification Kit II were purchased from
140 Dojindo (Japan).

141 **Cells and mice**

142 The human hepatocellular carcinoma cell line Hep-3B was obtained from Perccell (China) . The
143 cells were maintained in DMEM supplemented with 10% fetal bovine serum and 1 %
144 penicillin-streptomycin solution at 37°C in an atmosphere containing 5% CO₂. The animal experimental

protocol received approval from the Institutional Animal Care and Use Committee of Zhejiang Center of Laboratory Animals (ZJCLA) (ZJCLA-IACUC-20010242). Wild-type male BALB/c mice (GemPharmatech, China) aged 5 weeks were used for all *in vivo* experiments. The mice were housed under standard conditions, with an ambient room temperature of $22 \pm 2^{\circ}\text{C}$, humidity ranging from 40% to 70%, and a 12-hour light/dark cycle.

Gene datasets database

Autophagy related gene expression profile datasets was downloaded from the Human Autophagy Database (HADb).²⁷ Iron metabolism related gene expression profile datasets was downloaded from the article (doi: 10.3389/fnagi.2022.949083) reported by Xuefeng Gu and Donglin Lai, *et al.*⁵¹

***In vitro* analysis of therapeutic efficacy and functional mechanisms of drugs**

Cell viability assay

4000 per well Hep-3B cells were seeded into 96-well plates and cultured for 12 h. Then Hep-3B cells were subjected to the indicated drug formulations for 24 h (1. different concentrations of PPE; 2. 40 $\mu\text{g/mL}$ PPE combined with different concentrations of 3MA) under serum-free conditions. To assess cell viability, CCK8 analysis was performed by microplate reader using the CCK8 reagent, following the protocol provided by the manufacturer.

Cell proliferation assay

1.5 $\times 10^5$ per well Hep-3B cells were seeded into confocal imaging culture dishes and cultured for 12 h. Then Hep-3B cells were subjected to the indicated drug formulations for 22 h (PBS, PPE: 40 $\mu\text{g/mL}$) under serum-free conditions. And then added an equal volume of EdU working solution preheated at 37 $^{\circ}\text{C}$ and continued incubating for 2 h. To assess cell proliferation, fluorescence imaging analysis was performed by confocal laser scanning microscope using the BeyoClickTM EdU Cell Proliferation Kit with Alexa Fluor 488 and DAPI, following the protocol provided by the manufacturer.

Cell cycle assay

4.0 $\times 10^5$ per well Hep-3B cells were seeded into 60 mm cell culture dishes and cultured for 12 h. Then Hep-3B cells were subjected to the indicated drug formulations for 24 h (PBS, PPE: 40 $\mu\text{g/mL}$) under serum-free conditions. And then the cells were collected and fixed with pre-cooled 70% ethanol

for 12-24 h. To assess cell cycle, flow cytometry analysis was performed by flow cytometry using the Cell cycle staining Kit, following the protocol provided by the manufacturer.

Lactate dehydrogenase (LDH) release assay

4000 per well Hep-3B cells were seeded into 96-well plates and cultured for 12 h. Then Hep-3B cells were subjected to the indicated drug formulations for 24 h (different concentrations of PPE) under serum-free conditions. To assess cellular toxicity, extracellular LDH concentration analysis was performed by microplate reader using the LDH Cytotoxicity Assay Kit, following the protocol provided by the manufacturer.

Cell death or vitality assay

1.5×10^5 per well Hep-3B cells were seeded into confocal imaging culture dishes and cultured for 12 h. Then Hep-3B cells were subjected to the indicated drug formulations for 24 h (1. different concentrations of PPE; 2. PBS, PPE: 40 $\mu\text{g/mL}$, 3MA: 5 mM, NAC: 5 mM) under serum-free conditions. To assess cell toxicity, fluorescence imaging analysis was performed by confocal laser scanning microscope using the Calcein-AM/PI live/dead cell staining kit, following the protocol provided by the manufacturer.

Cell death and apoptosis assay

2.0×10^5 per well Hep-3B cells were seeded into 6-well plates and cultured for 12 h. Then Hep-3B cells were subjected to the indicated drug formulations for 48 h (1. PBS, PPE: 40 $\mu\text{g/mL}$; 2. PBS, PPE: 40 $\mu\text{g/mL}$, 3MA: 5 mM) under serum-free conditions. To assess cell death and apoptosis, flow cytometry analysis was performed by flow cytometry using the Annexin V FITC Apoptosis Detection Kit, following the protocol provided by the manufacturer.

Immunoblotting

2.0×10^5 per well Hep-3B cells were seeded into 6-well plates and cultured for 12 h. Then Hep-3B cells were subjected to the indicated drug formulations (Autophagy: PBS, PPE: 40 $\mu\text{g/mL}$, 3MA: 0.5 mM, CQ: 25 μM ; Apoptosis: PBS, PPE: 40 $\mu\text{g/mL}$, 3MA: 5 mM; Iron metabolism and IRS1: PBS, PPE: 40 $\mu\text{g/mL}$, 3MA: 5 mM) for 16-24 h (Apoptosis: cleaved caspase 3 24 h; Autophagy, iron metabolism and IRS1: 16 h) under serum-free conditions. Then cells were lysed. Protein lysates were separated by

SDS-PAGE and subsequently transferred to 0.22-0.45 μ m NC membranes. After that, subjected to standard immunoblotting procedures as previously described.

Autophagy assay

1.0 \times 10⁵ per well Hep-3B cells were seeded into the confocal imaging culture dishes. When the cell density reached about 50%, added Ad-mCherry-GFP-LC3B and infected for 24 h. Then removed and the infected Hep-3B cells were subjected to the indicated drug formulations for 16 h (PBS, PPE: 40 μ g/mL, 3MA: 0.5 mM, CQ: 25 μ M) under serum-free conditions. To assess autophagy activation, fluorescence imaging analysis was performed by confocal laser scanning microscope after stained with Hoechst 33342, following the protocol provided by the manufacturer.

Cell apoptosis assay by mitochondrial membrane potential analysis

2.0 \times 10⁵ per well Hep-3B cells were seeded into 6-well plates and cultured for 12 h. Then Hep-3B cells were subjected to the indicated drug formulations for 24 h (PBS, PPE: 40 μ g/mL, 3MA: 5 mM) under serum-free conditions. To assess cell apoptosis, flow cytometry analysis was performed by flow cytometry using the TMRE, following the protocol provided by the manufacturer.

ROS quantitative assay

2.0 \times 10⁵ per well Hep-3B cells were seeded into 6-well plates and cultured for 12 h. Then Hep-3B cells were subjected to the indicated drug formulations for 16 h (PBS, PPE: 40 μ g/mL, 3MA: 5 mM) under serum-free conditions. To assess ROS level, flow cytometry analysis was performed by flow cytometry using the CM-H2DCFDA (DCFH), following the protocol provided by the manufacturer.

SOD inhibition rate assay

4 \times 10⁵ per well Hep-3B cells were seeded into 60 mm cell culture dishes and cultured for 12 h. Then Hep-3B cells were subjected to the indicated drug formulations for 16 h (PBS, PPE: 40 μ g/mL, 3MA: 5 mM) under serum-free conditions. To assess SOD activity, intracellular SOD inhibition rate analysis was performed by microplate reader using the SOD Assay Kit, following the protocol provided by the manufacturer.

GSH concentration assay

4 \times 10⁵ per well Hep-3B cells were seeded into 60 mm cell culture dishes and cultured for 12 h.

226 Then Hep-3B cells were subjected to the indicated drug formulations for 16 h (PBS, PPE: 40 µg/mL,
227 3MA: 5 mM) under serum-free conditions. To assess GSH activity, intracellular GSH concentration
228 analysis was performed by microplate reader using the GSSG/GSH Quantification Kit II, following the
229 protocol provided by the manufacturer.

230 **Intracellular ferrous ion assay**

231 1.5×10⁵ per well Hep-3B cells were seeded into confocal imaging culture dishes and cultured for 12
232 h. Then Hep-3B cells were subjected to the indicated drug formulations for 16 h (PBS, PPE: 40 µg/mL,
233 3MA: 5 mM) under serum-free conditions. To assess ferrous ion concentration, fluorescence imaging
234 analysis was performed by confocal laser scanning microscope using FerroOrange, following the
235 protocol provided by the manufacturer.

236 **Intracellular ROS assay**

237 1.5×10⁵ per well Hep-3B cells were seeded into confocal imaging culture dishes and cultured for 12
238 h. Then Hep-3B cells were subjected to the indicated drug formulations for 16 h (PBS, PPE: 40 µg/mL,
239 3MA: 5 mM, DFO: 100 µM) under serum-free conditions. To assess ROS concentration, fluorescence
240 imaging analysis was performed by confocal laser scanning microscope using CM-H₂DCFDA (DCFH),
241 following the protocol provided by the manufacturer.

242 **Bioinformatics analysis**

243 **Acquisition of transcriptome data from cells**

244 5×10⁶ Hep-3B cells subjected to the indicated drug formulations for 16 h (PBS, PPE: 40 µg/mL,
245 under serum-free conditions) were collected. To acquire the transcriptome data, 1mL TRIzol was used to
246 lyse cells. The lysed samples were transported to Cosmos Wisdom for transcriptome sequencing.

247 **Differentially expressed genes analysis**

248 The online analysis tool GEO2R was used to identify the differentially expressed genes. Genes
249 with the specific cut-off criteria of $|\log_2(\text{FoldChange})| > 0$ and adjusted $p < 0.05$ were considered
250 differentially expressed genes and volcano plot was performed with R package. $\log_2(\text{FoldChange}) > 0$
251 was identified as up-regulated genes while $\log_2(\text{FoldChange}) < 0$ as down-regulated genes.

252 The online database Sangerbox (<http://vip.sangerbox.com/home.html>) was used to assess the
253 functions of differentially expressed genes, by conducting gene ontology (GO) analysis and kyoto
254 encyclopedia of genes and genomes (KEGG) pathway enrichment analysis. GO analysis encompassed
255 three fundamental aspects: biological process (BP), cellular component (CC) and molecular function
256 (MF). A significance threshold was set at Q value < 0.05 , and an enriched gene count ≥ 5 was chosen as
257 the criteria for statistical significance.

258 The differentially expressed genes in PPE group and the datasets from HADb database were
259 merged to identify the overlapping differentially expressed genes. The visual hierarchical cluster
260 analysis venn plot and heat map were performed with R package. To evaluate the protein-protein
261 interactions between the identified differentially expressed genes, the online database STRING
262 (<https://string-db.org/>) was used to perform the protein-protein interaction (PPI) network analysis.

263 An identified list of genes through the iron metabolism related datasets⁵¹ was selected. Gene set
264 enrichment analysis (GSEA) was conducted with R package, adjusted $p < 0.05$ was set as the criteria for
265 statistical significance. Then gene set variation analysis (GSVA) algorithm was used to score the gene
266 sets with R package, to evaluate the prospective alterations in biological functionality.

267 **Preparation and characterization of nanoformulations**

268 **Preparation of nanoformulations**

269 Initially, 4 mg of C16-cRGD was dissolved in 4 mL of a trifluoroacetic acid and acetonitrile
270 mixture (10: 90, v/v) and subsequently transferred to a 50 mL round-bottom flask for rotary evaporation
271 to produce a film. Subsequently, a second film was formed by 12 mg of lecithin, 4 mg of cholesterol,
272 and 4 mg of DSPE-PEG in 2 mL of chloroform in the aforementioned flask. Likewise, a third film was
273 created by dissolving 3 mg of 3MA in 3 mL of ethanol. Furthermore, 1 mg of PPE was dissolved in 1
274 mL of PBS buffer and introduced into the flask following ultrasonic vibrations. The resulting asAN-P/3
275 were purified using a dialysis bag (MWCO 300 KDa).

276 **Determination of 3MA ratio in asAN-P/3**

277 4000 per well Hep-3B cells were seeded into 96-well plates and cultured for 12 h. Then Hep-3B
278 cells were subjected to the indicated drug formulations for 24 h (different asAN-P/3 with different ratio

of 3MA / PPE, in which PPE was PPE 25 $\mu\text{g/mL}$) under serum presence conditions. To assess cell viability, CCK8 analysis was performed by microplate reader using the CCK8 reagent, following the protocol provided by the manufacturer.

Determination of cRGD ratio in asAN-P/3

1.5 $\times 10^5$ per well Hep-3B cells were seeded into confocal imaging culture dishes and cultured for 12 h. Then Hep-3B cells were subjected to the indicated drug formulations for 1 h (PBS and treatments with different ratio of cRGD / PPE in asAN-P/3, in which PPE was 20 $\mu\text{g/mL}$) under serum presence conditions. To assess cellular uptake ability, fluorescence imaging analysis was performed by confocal laser scanning microscope after stained with Hoechst 33342, following the protocol provided by the manufacturer.

Assessment of cRGD density in liposome

1 mL of C16-cRGD solution (2 mg/mL, dissolved in trifluoroacetic acid and acetonitrile mixture) and 10 μL of Rhodamine B NHS ester (1 mg/mL, dissolved in water) were mixed and co-cultured in 37 $^{\circ}\text{C}$ for 2 hours. The reaction production (C16-cRGD^{RB}) was purified by dialysis. Then, its standard curve was detected by ultraviolet-visible light spectrum. 1.5 mg/mL of liposome prepared by C16-cRGD^{RB} was diluted by mixed solution of trifluoroacetic acid and acetonitrile for 5 folds. Then, the cRGD density in liposome could be assessed by the ultraviolet-visible light spectrum of liposome solution.

Measurement of zeta potential, size and stability of nanoformulations

The size and zeta potential of the asAN-P/3 were determined using a Zetasizer Nano ZS90, while the morphology of the nanoparticles was characterized via transmission electron microscopy. The stability of asAN-P/3 was assessed by monitoring size changes at various time intervals.

Stability detection of asAN-P/3 in plasma

0.1 mL of asAN-P/3 was added to 0.9 mL plasma and co-cultured for different day in 37 $^{\circ}\text{C}$. Subsequently, the above-mentioned mixture was dialyzed by a dialysis bag for 6 h to eliminate free proteins and some small drugs. Then hydrated dimeters of purified asAN-P/3 in different days was detected by Nanoparticle Size and Zeta Potential Analyzer.

Measurement of the drug loading and encapsulation efficiency

The drug loading and encapsulation efficiency were calculated by analyzing the content of 3MA and PPE in the supernatant of the asAN-P/3 solution following centrifugation (12000 rpm, 30 min, 4°C). The concentration of 3MA was determined using ultraviolet-visible spectroscopy, whereas the concentration of PPE was quantified using BCA detection kits.

Measurement of drug release

To evaluate the drug release profile, 2 mL of asAN-P/3 were enclosed in a dialysis bag and immersed in 20 mL of PBS buffer containing Tween 80 (0.1%, w/v) at 37°C under oscillation conditions. At designated time points, 1 mL of buffer was sampled, and fresh buffer was replenished. The drug release kinetics were determined by analyzing the content of 3MA and PPE in collected PBS buffer.

Measurement of enzyme activity

266 µg/mL free PPE and released PPE from asAN-P/3 reacted with the elastase substrate N-Methoxysuccinyl-Ala-Ala-Pro-Val p-nitroanilide, respectively, following the protocol provided by the manufacturer. To assess enzyme activity, absorbance of 410nm was performed by microplate reader.

***In vitro* analysis of tumor cell targeting and therapeutic efficacy of nanoformulations**

Cellular uptake ability assay

1.5×10⁵ per well Hep-3B cells were seeded into confocal imaging culture dishes and cultured for 12 h. Then Hep-3B cells were subjected to the indicated drug formulations for 3 h (PBS, L-P^{Dil} and cL-P^{Dil}, the concentration of the PPE in nanoformulations was 7 µg/mL) under serum presence conditions. To assess cellular uptake ability, fluorescence imaging analysis was performed by confocal laser scanning microscope after stained with Hoechst 33342, following the protocol provided by the manufacturer.

Cell viability assay

4000 per well Hep-3B cells were seeded into 96-well plates and cultured for 12 h. Then Hep-3B cells were subjected to the indicated drug formulations for 24 h (PBS, free PPE, free 3MA, free PPE+3MA, cL-P, cL-3 and asAN-P/3, the concentration of the nanoformulations depended on PPE (2.50 µg/mL, 5.00 µg/mL, 6.25 µg/mL, 10.00 µg/mL, 12.50 µg/mL, 25.00 µg/mL, 40.00 µg/mL, 50.00

μg/mL), 3MA was 3.67 times that of PPE) under serum presence conditions. To assess cell viability, CCK8 analysis was performed by microplate reader using the CCK8 reagent, following the protocol provided by the manufacturer.

Immunoblotting

2.0×10⁵ per well Hep-3B cells were seeded into 6-well plates and cultured for 12 h. Then Hep-3B cells were subjected to the indicated drug formulations for 16 h (PBS, cL-P, cL-3 and asAN-P/3, the concentration of the PPE in nanoformulations was 15 μg/mL, 3MA was 3.67 times of PPE) under serum presence conditions. Then cells were lysed. Protein lysates were separated by SDS-PAGE and transferred to 0.22-0.45 μm NC membranes. After that, subjected to standard immunoblotting procedures as previously described.

Cell death and apoptosis assay

2.0×10⁵ per well Hep-3B cells were seeded into 6-well plates and cultured for 12 h. Then Hep-3B cells were subjected to the indicated drug formulations for 24 h (PBS, free PPE+3MA, cL-P, cL-3 and asAN-P/3, the concentration of the PPE in nanoformulations was 0.01 μg/mL, 3MA was 3.67 times of PPE) under serum presence conditions. To assess cell death and apoptosis, flow cytometry analysis was performed by flow cytometry using the Annexin V FITC Apoptosis Detection Kit, following the protocol provided by the manufacturer.

***In vivo* analysis of tumor targeting and therapeutic efficacy of nanoformulations**

***In vivo* tumor targeting and biodistribution assay**

Hep-3B tumor-bearing BALB/c mice were generated through the injection of 2 ×10⁶ Hep-3B cells subcutaneously on the right side (*n* = 3). Once the tumor volume reached approximately 80-100 mm³, intravenous administration of PPE^{ICG}, L-P^{ICG} and cL-P^{ICG} (with a dosage of 30.25 μg for PPE) was performed on the mice. The fluorescence images of the mice were captured at various time points using an *in vivo* fluorescence imaging system. At the end, tumor tissues, heart, liver, spleen, lungs and kidneys of mice were obtained. The fluorescence images of the tissues were captured using an *in vivo* fluorescence imaging system.

***In vivo* tumor inhibition**

360 Hep-3B tumor-bearing BALB/c mice were generated through the injection of 2×10^6 Hep-3B cells
361 subcutaneously on the right side. Once the tumor volume reached approximately 100 mm^3 , the Hep-3B
362 tumor-bearing mice were randomly divided into five groups ($n = 6$). On day 0, the mice were
363 intravenously administered with PBS, free PPE, free PPE+3MA, cL-P, cL-3 or asAN-P/3, respectively.
364 These treatments were repeated every two days for a total of five administrations, with a dosage of 60.5
365 μg for PPE and $222 \mu\text{g}$ for 3MA. Tumor volume was calculated using the standard formula: $V = (\text{tumor}$
366 $\text{length}) \times (\text{tumor width})^2 / 2$. Tumor volume was recorded every 2 days unless the mice displayed signs of
367 prolonged distress, interference with normal movement or access to food and water, ulceration of the
368 tumor, or when the tumor reached a size larger than 20 mm in diameter. On day 10, the tumors were
369 harvested for photograph, tumor weight, H&E assay, Ki67 histochemistry assay, p62 histochemistry
370 assay, LC3B histochemistry assay and TUNEL assay using One Step TUNEL Apoptosis Assay Kit.

371 ***In vivo* survival observation**

372 Hep-3B tumor-bearing BALB/c mice were generated through the injection of 2×10^6 Hep-3B cells
373 subcutaneously on the right side. Once the tumor volume reached approximately 100 mm^3 , the Hep-3B
374 tumor-bearing mice were randomly divided into five groups ($n = 10$). On day 0, the mice were
375 intravenously administered with PBS, free PPE, free PPE+3MA, cL-P, cL-3 or asAN-P/3, respectively.
376 These treatments were repeated every two days for a total of five administrations, with a dosage of 60.5
377 μg for PPE and $222 \mu\text{g}$ for 3MA. Tumor volume was calculated using the standard formula: $V = (\text{tumor}$
378 $\text{length}) \times (\text{tumor width})^2 / 2$. Tumor volume was recorded every 2 days unless the mice displayed signs of
379 prolonged distress, interference with normal movement or access to food and water, ulceration of the
380 tumor, or when the tumor reached a size larger than 20 mm in diameter, until mice in all groups except
381 asAN-P/3 group were recorded death.

382 ***In vivo* analysis of biosafety of nanoformulations**

383 Healthy Balb/c mice ($n = 3$) were administered with PBS, free PPE, free PPE+3MA, cL-P, cL-3 or
384 asAN-P/3, respectively every two days for a total of five treatments (with a dosage of $60.5 \mu\text{g}$ for PPE
385 and $222 \mu\text{g}$ for 3MA). On day 10, blood samples were collected for blood biochemistry analysis, which
386 included measurements of alanine transaminase (ALT), aspartate aminotransferase (AST), urine

nitrogen (UREA), creatinine (CRE-J) and blood routine analysis, which included measurements of red blood cells (RBC), hemoglobin (HGB), mean corpuscular hemoglobin (MCH), hematocrit (HCT), mean corpuscular volume (MCV), platelets (PLT), mean platelet volume (MPV), white blood cells (WBC), neutrophils and lymphocytes. Additionally, the main organs (heart, liver, spleen, lung and kidney) of the mice were harvested for histological examination using H&E assay.

Statistical analysis

The data analysis was performed using GraphPad Prism version 10. Statistical analysis was conducted using unpaired t-tests or paired t-tests for comparisons between two groups, while one-way analysis of variance (ANOVA) was used for comparisons involving three or more groups. Half maximal inhibitory concentration (IC₅₀) of drugs and nanoformulations analysis was performed using the Nonlinear regression (Curve fit). Kaplan-Meier survival curves were used to present animal survival, and statistical analysis was performed using the Log-rank (Mantel-Cox) test. A statistical significance threshold of $p < 0.05$ was applied. In the figures, the symbols * denoted $p < 0.05$, ** denoted $p < 0.01$, *** denoted $p < 0.001$, **** denoted $p < 0.0001$ and ns indicated no statistical significance.

Results and Discussion

Autophagy Activation in HCC by PPE

First, Hep-3B cells were treated with different concentrations of the alternative of ELANE, PPE. The inhibitory effect of PPE on cell proliferation was observed to increase within the concentrations range of 3.13 to 12.5 $\mu\text{g/mL}$. However, this effect reached a plateau at higher concentrations (25-400 $\mu\text{g/mL}$) (**Figure 2A**). To investigate this observation, viability staining and apoptosis analysis were conducted. Results showed that at the high concentrations (400 $\mu\text{g/mL}$) of PPE, there was no significant increase in the number of propidium iodide (PI)-stained cells, yet a noticeable reduction in Calcein-stained cells was noted (**Figure S1**, Supporting Information). These results suggested that PPE could impede the cell viability rather than induce cell death. This was further supported by the absence of a significant change in the apoptosis rate (**Figure S2**, Supporting Information). Additionally, the lactate dehydrogenase (LDH) release assay revealed no significant difference in extracellular LDH

414 levels of HCC cells treated with different concentrations of PPE (3.13-150 $\mu\text{g/mL}$) (**Figure S3**,
415 Supporting Information). This observation indicated a lack of substantial cytotoxicity associated with
416 PPE treatment. Overall, these findings demonstrated that PPE could inhibit HCC cell viability without
417 promoting cell death.

418 To further investigate the mechanism underlying the observed inhibitory effect, Edu assay was
419 conducted. A notable reduction in Edu fluorescence within the PPE treated group was observed,
420 suggesting that PPE could effectively inhibit cell proliferation. Furthermore, cell cycle analysis
421 demonstrated a significant increase in the proportion of cells in the G0/G1 phase. This indicated that
422 PPE inhibited the cell proliferation by arresting HCC cells in the quiescent phase (**Figures S4-S5**,
423 Supporting Information). Collectively, these findings illustrated that the anti-tumor effect of PPE on
424 Hep-3B cells primarily arose from the inhibition of cell proliferation rather than the induction of
425 apoptosis.

426 In order to explore the functional mechanism of the limited therapeutic efficacy of PPE against
427 hepatocellular carcinoma (HCC), transcriptome sequencing was performed. Firstly, we identified 3550
428 differentially expressed genes (DEGs), including 1000 up-regulated DEGs (**Figure 1A**). Subsequently,
429 gene ontology (GO) and kyoto encyclopedia of genes and genomes (KEGG) analysis were used to
430 perform biological enrichment of the identified up-regulated DEGs.

431 KEGG analysis showed that autophagy was the third most significant differential pathway. It is
432 worth noting that the first two differential pathways are tightly associated with the autophagy process
433 (**Figure 1B**) [25]. In addition, GO analysis showed significant enrichment of autophagy in both
434 biological process (BP) and cellular component (CC). Besides, the other enrichment signals and
435 functions were closely associated with autophagy (**Figure 1C**) [25], suggesting the activated autophagic
436 signal in PPE group. These results identified the same functional pathway, autophagy, in PPE group.

437 Protective autophagy plays an important role in conferring drug resistance and promoting tumor
438 development in HCC, through the clearance of damaged or redundant peroxisomes, organelles and
439 abnormal proteins [26]. Based on these, all DEGs in PPE group were merged with the autophagy related
440 genes and identified 67 overlapping DEGs related to autophagy (**Figures 1D-1E**) [27]. Furthermore,

protein-protein interaction (PPI) network analysis demonstrated that almost all of the identified genes had interaction (**Figure 1F**), jointly affecting the level of autophagy. These results indicated the important potential role autophagy played in PPE therapy.

In light of this, Hep-3B cells were transfected with Ad-mCherry-GFP-LC3B to evaluate autophagy. Results showed significant increases in both green (indicative of the early autophagy stage) and predominately red fluorescence (indicative of the full autophagy stage) in cells treated with PPE. When combined with 3MA, both fluorescence signals were notably reduced, whereas in combination with chloroquine (CQ), they were significantly enhanced (**Figure 2B, Figure S6**, Supporting Information). These observations implied that the autophagy induced by PPE could be suppressed by both the early inhibitor 3MA and the late inhibitor CQ. Specifically, 3MA impeded autophagosome formation, leading to a decreased level of LC3B. While CQ hindered autophagolysosome formation and the degradation of the metabolites, consequently resulting in the accumulation of LC3B [28]. This indicated that PPE could induce a complete autophagic flux in HCC cells.

In addition, the increase in LC3B II / LC3B I, and the degradation of p62 are pivotal for assessing activated autophagy [29]. Results showed a substantial decrease in p62 and an increase in LC3B II / LC3B I, alongside elevated levels of Atg7 and Atg5 in cells treated with PPE [29]. These changes were reversible upon treatment with 3MA or CQ (**Figure 2C, Figures S7-S8**, Supporting Information). This suggested that PPE could activate the autophagy signaling pathway, with the degradation of the autophagy substrate. Particularly, 3MA inhibited the expression of LC3B, while CQ increased the accumulation of LC3B and p62 by impeding degradation [28]. Based on the aforementioned findings, it could be concluded that PPE activated complete autophagic flux in HCC cells, involving the process from autophagosome formation to autophagolysosome maturation, with the subsequent degradation of cellular metabolites.

3MA Enhanced the Efficacy of PPE-mediated Tumor Therapy

To elucidate the role of PPE-induced autophagy in HCC, Hep-3B cells were treated with PPE along with the autophagy inhibitor 3MA. Cell viability was significantly inhibited in the combination group

(**Figure 2D**). This observation suggested that inhibiting autophagy may enhance the cytotoxicity of PPE in HCC. Subsequently, apoptosis analysis revealed a significantly elevated rate of apoptosis (**Figures 2E-2F**), especially the early apoptosis, in the combination group (**Figure S9**, Supporting Information). In addition, the substantial activation of cleaved caspase 3 (**Figure 2G**, **Figure S10**, Supporting Information) and the significant reduction in mitochondrial membrane potential (**Figures 2H-2I**) further supported the enhancement of cytotoxicity by the addition of 3MA [30,31]. Collectively, these results indicated that the addition of an autophagy inhibitor could significantly promote cell death in HCC, highlighting the protective role of autophagy in the PPE treatment.

Subsequently, we investigated the underlying mechanism of the combination group in HCC. Prior studies have shown that PPE can induce cell death by disrupting mitochondria and generating ROS through CD95 cleavage [11]. Our assessment of intracellular ROS levels showed a significant increase in the PPE group, with no discernible change in the 3MA group. Interestingly, the combination group exhibited a markedly elevated level of ROS compared to the individual treatment groups (**Figures 3A-3B**), indicating a substantial induction of oxidative stress in HCC in combination group.

Notably, tumor cells have the capacity to counteract ROS through the activation of protective autophagy and antioxidant pathways. These pathways include a variety of antioxidant effectors such as superoxide dismutase (SOD) [32], glutathione (GSH) [33], nuclear factor erythroid 2-related factor 2 (Nrf2) [34], hypoxia-inducible factor 1 α (HIF1 α) and the spliced activation form of unfolded protein response transcription factor X-box-binding protein 1 (s-XBP1) [35,36]. These effectors effectively remove ROS, maintain cellular homeostasis, inhibit cell death, and contribute to drug resistance.

Therefore, we assessed the changes in antioxidant signals. Results of SOD inhibition rate and GSH level revealed an increased consumption of SOD and GSH in both the PPE and 3MA group, while the combination group showing the most significant depletion (**Figure 3D**, **Figure S11**, Supporting Information). In light of the previous findings, it could be concluded that the consumption of SOD and GSH inhibited the cell death in the PPE group. However, it enhanced the cell death in the combination group. This is due to the fact that the consumption of SOD and GSH prevents the ROS mediated cell death while the exhaustion (excessive consumption, high degree of consumption) of SOD and GSH

promotes cell apoptosis [37,38].

Further analysis showed a substantial up-regulation of s-XBP1 and HIF1 α in the PPE group, with no significant change of Nrf2. Notably, the addition of 3MA led to a significant suppression of these three factors (**Figure 3E**, **Figure S12**, Supporting Information). This observation implied that HIF1 α and s-XBP1, rather than Nrf2, functioned as the primary antioxidants in the PPE group. This is attributed to the suppressive effects of PPE and XBP1 on the expression of Nrf2 [39,40], resulting in insufficient Nrf2-mediated antioxidant capacity and activation of alternative antioxidant factors [41]. These findings illustrated that although PPE raised intracellular oxidative stress by generating ROS, tumor cells were capable to mitigate the stress and maintain homeostasis through the activation of antioxidant pathways.

However, the limitation could be reversed by 3MA. It exerts inhibitory effects on the activity of SOD, GSH [42], as well as the expression of HIF1 α [43], Nrf2 and XBP1 [44,45], to promote oxidative stress mediated cell death. In light of this, we investigated the important role of ROS in cancer cell death by utilizing N-acetylcysteine (NAC) to remove ROS. Remarkably, we observed a significant increase in cell death in combination group, which could be reversed by NAC (**Figure 3C**). These findings indicated that 3MA had the potential to enhance the therapeutic efficacy of PPE through oxidative stress *in vitro*.

Building upon this premise, we investigated the origins of ROS induced by the combination group in HCC. It has been noted that the expression of CD95 is low in HCC, especially in the late stage, with silenced function in HCC (**Figure S13**, Supporting Information) [46], suggesting the possibility of alternative mechanisms contributing to ROS generation. Liver serves as the predominant iron pools in the body owing to its enormous storage of iron and proteins containing Fe-S, rendering it highly reactive toward ROS [47]. As a result, the impact of iron metabolism on oxidative stress in HCC has garnered increasing attention in recent years [48]. In addition, ELNAE has been shown to regulate breast cancer progression by degrading insulin receptor substrate 1 (IRS1) [49], the loss of which leads to a higher iron level in the liver [50]. We observed a similar degradation of IRS1 in cells treated with PPE (**Figure S14**, Supporting Information).

522 Thereby, it is reasonable to hypothesize that iron metabolism may contribute to the efficacy of
523 PPE-mediated therapy in HCC. Therefore, we obtained datasets of genes related to iron metabolism [51].
524 Based on it, we performed gene set enrichment analysis (GSEA) and gene set variation analysis (GSVA)
525 for the up-regulated DEGs in PPE group. GSEA analysis found that PPE significantly up-regulated iron
526 ion homeostasis (**Figure 3F**). Moreover, GSVA signature score analysis showed five significantly
527 up-regulated iron metabolism related pathways in PPE group, with distinct upward trends in the other
528 two pathways (**Figure 3G**). These results indicated that iron metabolism had an important potential role
529 in PPE therapy.

530 ROS produced by iron metabolism primarily originate from ferrous ions [48]. Hence, we assessed
531 the intracellular ferrous ions content and observed a significant increase in cells treated with PPE, which
532 was further elevated when combined with 3MA (**Figure 3H**). Notably, iron overload down-regulates
533 transferrin receptor 1 (TfR1, also known as CD71) and divalent metal transporter 1 (DMT1) through
534 negative feedback regulation, while up-regulating Ferritin to bind excess iron [52-54], thereby reducing
535 the intracellular iron.

536 Consequently, we identified a significant reduction in the expression of CD71 and an increase in
537 the expression of Ferritin in cells treated with PPE. When combined with 3MA, the expression of CD71
538 significantly decreased, while the expression of Ferritin exhibited an increasing trend (**Figures 3I-3J**,
539 **Figure S15**, Supporting Information). Nevertheless, there was no discernible change in the expression of
540 DMT1 across the different groups (**Figure S16**, Supporting Information). This is attributed to the fact
541 the down-regulation of DMT1 is the consequence of prolonged iron overload rather than a short-term
542 variation [55]. These findings suggested that PPE could induce iron overload in HCC, with a higher
543 level in the combination group.

544 Subsequently, to investigate the important role of iron metabolism in the oxidative stress induction
545 in HCC, deferoxamine (DFO) was utilized to eliminate excess ferrous ions. We observed a noticeably
546 elevated level of ROS in the combination group, which was markedly reduced by DFO (**Figure 3K**),
547 This observation indicated the crucial role of iron in ROS generation in the combination group. Overall,
548 the aforementioned findings illustrated that PPE could induce oxidative stress by regulating iron

metabolism in HCC, with an amplified effect in combination with 3MA. It is noteworthy that the regulatory effect of the therapy on oxidative stress induced by iron metabolism is not a unilateral outcome, but rather the result of a comprehensive interplay involving mitochondrial destruction [56], autophagy [54], iron-related proteins metabolism and IRS1 degradation [50,57].

In summary, although the alternative of ELANE, PPE, inhibited the proliferation and induced oxidative stress through iron overload in HCC, its efficacy was constrained by the cellular activation of protective autophagy and antioxidant pathways, which protected HCC from death. Conversely, the addition of 3MA could not only inhibited protective autophagy, but also the antioxidant pathways, thereby synergistically sensitizing the toxicity of PPE in HCC (**Figure 3L**).

Preparation and Characterization of Augmented Sensitized Artificial Activated Neutrophil

The alternative of ELANE, PPE, could be inactivated by serum (**Figure S17**, Supporting Information) owing to the natural protease inhibitors in the blood and consumed by degrading extracellular connective tissue [14-16]. Moreover, considering the high demand of cells from patients in neutrophil-based carrier and the fact that their targeting ability depended on the level of inflammatory chemotaxis signaling in the tumor [6]. To solve above problems, we prepared a targeted liposomal nanoplatfrom with cRGD via the rotary evaporation method (**Figure 4A**). Among them, phospholipid, cholesterol and DSPE-PEG consisted of the framework nanoplatfrom in asAN-P/3. C16-cRGD was utilized as the targeting peptide modified on the asAN-P/3 targeting HCC tumor cell. Besides, PPE and 3MA loaded in asAN-P/3 were delivered through the cRGD modified nanoplatfrom into HCC cell, as the effective combination drugs, synergistically improving tumor cell death.

To optimize component ratios, 3MA loading ratios were first assessed for nanoparticle cytotoxicity, revealing a dose-dependent increase that plateaued at 3:1 (3MA:PPE) (**Figure S18**, Supporting Information). Subsequently, cRGD ratios were evaluated for cellular targeting, showing enhanced uptake until saturation at 4:1 (cRGD:PPE) (**Figure S19**, Supporting Information). Based on these results, the therapeutic nanoparticle asAN-P/3 was synthesized for further study.

The density of cRGD in asAN-P/3 is about 0.144 g/cm³ (**Figure S20**, **Table S1**, Supporting

Information), which was detected by fluorescence labeling and absorption spectroscopy detection. The loading and encapsulation efficiency for PPE were determined to be 2.16% and 60.5%, respectively, while those for 3MA were 7.93% and 74.0%. The hydrodynamic diameter and surface zeta potential of augmented sensitized artificial activated neutrophil asAN-P/3 was 111.53 ± 9.17 nm and -15.73 ± 0.21 mV, respectively, which were similar to other control nanomedicines (**Figures 4B-4C**).

The asAN-P/3 exhibited typical vesicle structures with a phospholipid bilayer coating. The dry diameter of these particles was approximately 100 nm, which was smaller than hydrated diameter due to particle contraction (**Figure 4C, Figure 4E**). Moreover, the diameter of asAN-P/3 remained constant in phosphate buffer solution (PBS) buffer at pH 7.4 over a period from 0 to 72 h (**Figure 4D**), demonstrating excellent stability under neutral conditions. We also detected the hydrated diameter of asAN-P/3 in plasma in different days. Results showed that its diameter is slightly larger than that in water, which may be a result of surface protein absorption of asAN-P/3 in plasma. In addition, the diameter of asAN-P/3 didn't change obviously indicating it remain stable in plasma (**Figure S21**, Supporting Information).

To evaluate the release kinetics of 3MA and PPE, the augmented sensitized artificial activated neutrophil asAN-P/3 was encapsulated within a dialysis bag with a molecular weight cut-off (MWCO) of 300 kDa and subsequently immersed in a PBS containing Tween 80 (0.1%, w/v) at 37°C under oscillation conditions. The results showed a rapid release of PPE, with 79.6% released within the initial 24 h. The released PPE retained $94.79 \pm 0.86\%$ enzymatic activity compared to free PPE, indicating preserved functionality post-nanoformulation (**Figure S22**, Supporting Information). In contrast, 3MA exhibited a sustained-release profile, with only 49.2% released within the same period (**Figure 4F**). This difference in release rates may be attributed to the differing solubility properties, where PPE is more hydrophilic and 3MA is more hydrophobic.

***In Vitro* Evaluation of Tumor Targeting and Therapeutic Potential of asAN-P/3**

Aiming to investigate the intracellular delivery capability and therapeutic efficacy of the augmented sensitized artificial activated neutrophil on HCC *in vitro*, we initially treated Hep-3B cells with

Dil-labeled nanomedicines. The cL-P group exhibited the most pronounced fluorescence signal (**Figure 5A**), indicating enhanced cellular uptake ability. Subsequently, to assess the therapeutic efficacy of asAN-P/3 *in vitro*, Hep-3B cells were treated with different drugs. We observed the highest level of toxicity in the asAN-P/3 group (**Figure 5B**), with a significantly reduced IC₅₀ of 117.6 ng/mL (**Figure S23**, Supporting Information). Moreover, asAN-P/3 significantly increased the apoptosis rate of HCC (**Figures 5D-5E**), especially the early apoptosis (**Figure S24**, Supporting Information).

Furthermore, an analysis of autophagy-related proteins revealed that the cL-P group showed increased conversion of LC3B, with substantial degradation of p62. These effects could be reversed by 3MA in the asAN-P/3 group, suggesting 3MA inhibited the up-regulated autophagy induced by PPE. Notably, the cL-3 group exhibited marked up-regulation of p62 alongside a moderate increase in LC3B expression (**Figure 5C**, **Figure S25**, Supporting Information), indicating that the inhibitory effect on autophagy caused by 3MA could cumulatively disrupt the cellular homeostasis, thereby slightly activating autophagy when the inhibitory effect was eliminated [58]. Collectively, these findings demonstrated that the augmented sensitized artificial activated neutrophil asAN-P/3 not only facilitated efficient intracellular delivery, but also greatly enhanced cytotoxicity against HCC by modulating autophagy *in vitro*.

***In Vivo* Evaluation of Tumor Targeting and Therapeutic Potential of asAN-P/3**

Building upon the demonstrated excellent cellular uptake ability of cL-P *in vitro*, we attempted to investigate the targeting ability and biodistribution of cL-P *in vivo*, as depicted in **Figure 6A**. At 8, 24, and 48 hours post intravenous injection, a significant increase in tumor accumulation was observed within the cL-P group (**Figures 6B-6C**). These observations suggested that nanomization and cRGD modification significantly enhanced the targeting specificity.

Subsequently, the major organs and tumor tissues from the experimental mice were collected for further biodistribution analysis. Results showed a significant increase in fluorescence within the tumor tissues of the cL-P group, further indicating the target capability of nanoliposome modified with cRGD (**Figure 6B**, **Figure 6D**). Notably, a notable accumulation of PPE was observed in the blood-rich organs,

particularly the liver (**Figure 6B, Figure 6D**). However, in conjunction with **Figure 6B**, it became evident that the fluorescence intensity in the liver decreased over time, attributed to the gradual clearance of the nanomedicine by systemic circulation mechanisms [59].

Encouraged by the excellent targeting ability of the augmented sensitized artificial activated neutrophil, we proceeded to investigate therapeutic efficacy of asAN-P/3 *in vivo*. Mice were treated with PBS, free PPE, free PPE+3MA, cL-P, cL-3 or asAN-P/3, as shown in **Figure 7A**. Tumor growth analysis revealed no significant inhibition in the free PPE group compared to PBS controls, while free PPE+3MA, cL-P, and cL-3 groups exhibited moderate suppression, indicating enhanced therapeutic efficacy through nanoformulation. Notably, the asAN-P/3 group achieved the highest tumor inhibition rate ($80.09 \pm 7.35\%$, **Figures 7B-7C, Figures S26A-S26B, Supporting Information**), with tumor weight measurements corroborating this pronounced suppression (**Figure 7D, Figures S26C, Supporting Information**). These highlighted the substantial suppression in the asAN-P/3 group.

Hematoxylin-eosin (H&E) staining results showed that tumors in the asAN-P/3 group displayed the highest levels of tumor cell apoptosis and necrosis, compared to the other groups (**Figure 7F**). These findings indicated that asAN-P/3 possessed potent anti-tumor capabilities and effectively suppressed tumor progression. Based on these observations, we assessed the proliferation ability and apoptosis degree of tumor tissues using Ki67 immunohistochemistry and TUNEL assay [60,61]. The Ki67 immunohistochemistry results demonstrated that compared to other groups, the asAN-P/3 group showed the best effect in tumor proliferation inhibition (**Figures 7E-7F**). Additionally, the TUNEL assay results indicated that in comparison to the PBS group, the free PPE+3MA, cL-P and cL-3 groups showed negligible apoptosis, while the asAN-P/3 group exhibited significantly up-regulated apoptosis, both in terms of the proportion of apoptosis (**Figures 7G-7H**) and the apoptotic area (**Figure S27, Supporting Information**). These findings demonstrated that the augmented sensitized artificial activated neutrophil asAN-P/3 could effectively inhibit tumor cell proliferation while significantly promoting tumor apoptosis, thereby synergistically enhancing the therapeutic efficacy against tumors.

Additionally, immunohistochemical staining of LC3B and p62 was performed on the tumor tissues underlying the mechanism *in vivo*. The group treated with free PPE+3MA did not show obvious

regulatory effects compared to the PBS group, potentially due to the lack of specific targeting. Compared to the cL-P group, asAN-P/3 group exhibited significantly down-regulated LC3B and up-regulated p62, indicating that 3MA could effectively inhibit autophagy induced by PPE (**Figure 7F**, **Figure S28**, Supporting Information).

Inspired by the excellent short-term anti-tumor ability of the augmented sensitized artificial activated neutrophil, we monitored the long-term survival rates of asAN-P/3-treated mice. Survival curves revealed slight improvement in the free PPE group compared to PBS controls, with moderate enhancement in the free PPE+3MA, cL-P, and cL-3 groups. Notably, asAN-P/3 achieved the highest survival rate, demonstrating its enhanced efficacy in prolonging survival (**Figure 7I**, **Figure S29**, Supporting Information). Collectively, these findings illustrated that the augmented sensitized artificial activated neutrophil asAN-P/3 displayed precise HCC targeting, outstanding anti-tumor efficacy and prolonged survival ability through the regulation of autophagy *in vivo*.

***In Vivo* Bio-Compatibility of asAN-P/3**

In vivo bio-compatibility of the augmented sensitized artificial activated neutrophil asAN-P/3 was further assessed. Body weights of mice were monitored throughout the treatment period. The results showed no significant weight loss observed in any of the experimental groups (**Figure 8A**, **Figure S30A**, **Supporting Information**). Blood biochemistry revealed no statistically significant differences in aspartate transaminase (AST) and alanine transaminase (ALT) levels between the asAN-P/3 group and the control group (**Figure 8B**, **Figures S30B-C**, **S31A**, Supporting Information), indicating preserved hepatic function [62]. Similarly, renal markers creatinine (CRE-J) and urea (UREA) showed no alterations across groups (**Figure 8C**, **Figures S30D-E**, **S31B**, Supporting Information) [62], confirming systemic safety. Histological examination on the liver, heart, lung, spleen and kidney revealed no signs of tissue toxicity in any of the experimental groups (**Figure 8D**). Additionally, key hematological parameters (white blood cell count, red blood cells, hemoglobin, coagulation) showed no significant differences in any of the experimental groups (**Figures 8E-8H**, **Figures S32-S33**, Supporting Information), indicating normal hematological function. Nonetheless, the non-targeting free PPE may be

taken up by normal cells, causing a mild inflammatory response that in turn causes an increase in neutrophils in the free PPE+3MA group and decrease in lymphocytes in the free PPE group [63], which was not observed in the nanomedicine groups (**Figures S32E, S33B**, Supporting Information).

In summary, these findings suggested that the augmented sensitized artificial activated neutrophil asAN-P/3 exhibited no significant systemic toxicity, indicating its potential as a promising therapeutic agent with superior bio-compatibility for HCC in the future.

Conclusion

In this work, we discovered a limited therapeutic efficacy of the activated neutrophil killing effector mimicker, PPE, in HCC. It activated protective autophagy and antioxidative signals to protect tumor cells from death, which limited its therapeutic potential. Importantly, the incorporation of 3MA, an autophagy inhibitor, sensitized PPE by enhancing iron-related ROS-mediated cell destruction induced by PPE. Subsequently, an augmented sensitized artificial activated neutrophil asAN-P/3 was prepared to target HCC and improve the therapeutic efficacy, overcoming the constraint in neutrophil-based and artificial neutrophil related anti-tumor therapy (**Scheme 2**). *In vitro* and *in vivo* evidence indicated the precise targeting ability, excellent therapeutic efficacy, prolonged survival and favorable bio-compatibility. Our study contributes valuable insights for the advancement and application in clinical translation of neutrophil-related therapeutic strategies in oncology in the future.

Abbreviations

ELANE: neutrophil elastase; PPE: porcine pancreatic elastase; HCC: hepatocellular carcinoma; ROS: reactive oxygen species; 3MA: 3-Methyladenine; cRGD: cyclic arginine glycine aspartate peptide; PI3K: phospholipase-like III enzymes; PBS: phosphate buffer solution; NAC: N-acetylcysteine; CCK8: Cell Counting Kit-8; TMRE: tetramethylrhodamine ethyl ester; CQ: chloroquine; DFO: deferoxamine; HADb: Human Autophagy Database; LDH: lactate dehydrogenase; IRS1: insulin receptor substrate 1; SOD: superoxide dismutase; GSH: glutathione; GSSG: oxidized glutathione; GO: gene ontology;

710 KEGG: kyoto encyclopedia of genes and genomes; BP: biological process; CC: cellular component; MF:
711 molecular function; PPI: protein-protein interaction; GSEA: gene set enrichment analysis; GSVA: gene
712 set variation analysis; H&E: Hematoxylin-eosin; ALT: alanine transaminase; AST: aspartate
713 aminotransferase; UREA: urine nitrogen; CRE-J: creatinine; RBC: red blood cells; HGB: hemoglobin;
714 PLT: platelets; MPV: mean platelet volume; WBC: white blood cells; ANOVA: one-way analysis of
715 variance; PI: propidium iodide; DEGs: differentially expressed genes; Nrf2: nuclear factor erythroid
716 2-related factor 2 ;HIF1 α : hypoxia-inducible factor 1 α ; s-XBP1: spliced X-box-binding protein 1;
717 TfR1(same as CD71): transferrin receptor 1; DMT1: divalent metal transporter 1; MWCO: molecular
718 weight cut-off; TEM: transmission electron microscopy; CLSM: confocal laser scanning microscopy;
719 TUNEL: TdT-mediated dUTP nick end labeling

720

721 **Acknowledgments**

722 We would like to express our gratitude to Biorender (biorender.com) for its images used in our figures.
723 We thank the Chemistry Instrumentation Center, Zhejiang University for characterization support,
724 including Fang Chen for help with TEM analysis.

725

726 **Funding Statement**

727 We gratefully acknowledge the financial support by Key Research and Development Program of
728 Zhejiang Province (Program No. 2024C03143), National Natural Science Foundation of China (No.
729 U23A202181, 82072650, 82272860), Central Guidance on Local Science and Technology Development
730 Fund of Zhejiang Province (2023ZY1017), Key Project of Traditional Chinese Medicine Science and
731 Technology Plan of Zhejiang Province(GZY-ZJ-KJ-24077), Fundamental Research Funds for the
732 Central Universities (No. 226-2023-00038), Postdoctoral Research Funding Project of Zhejiang
733 Province (No. ZJ2022077), Special Financial Support for Zhejiang Traditional Chinese Medicine
734 Innovation Teams, Postdoctoral Fellowship Program of CPSF (No. GZC202415120).

735

Conflict of Interest Disclosure

The authors report no conflicts of interest in this work.

References

1. Llovet JM, Kelley RK, Villanueva A, Singal AG, Pikarsky E, Roayaie S, et al. Hepatocellular carcinoma. *Nat Rev Dis Primers*. 2021; 7: 6.
2. Center MM, Jemal A. International trends in liver cancer incidence rates. *Cancer Epidemiol Biomarkers Prev*. 2011; 20: 2362–8.
3. Llovet JM, Pinyol R, Yarchoan M, Singal AG, Marron TU, Schwartz M, et al. Adjuvant and neoadjuvant immunotherapies in hepatocellular carcinoma. *Nat Rev Clin Oncol*. 2024; 21: 294–311.
4. Yang X, Yang C, Zhang S, Geng H, Zhu AX, Bernards R, et al. Precision treatment in advanced hepatocellular carcinoma. *Cancer Cell*. 2024; 42: 180–97.
5. Linde IL, Prestwood TR, Qiu J, Pilarowski G, Linde MH, Zhang X, et al. Neutrophil-Activating therapy for the treatment of cancer. *Cancer Cell*. 2023; 41: 356–72.e10.
6. Gao P, Zou D, Zhao A, Yang P. Design and optimization of the circulatory cell-driven drug delivery platform. *Stem Cells Int*. 2021; 2021: 8502021.
7. Jiang W, Xu H, Gao Z, Wu Z, Zhao Z, Wang J, et al. Artificial neutrophils against vascular graft infection. *Adv Sci (Weinh)*. 2024; 11: e2402768.
8. Chang Y, Cai X, Syahirah R, Yao Y, Xu Y, Jin G, et al. Car-neutrophil mediated delivery of tumor-microenvironment responsive nanodrugs for glioblastoma chemo-immunotherapy. *Nat Commun*. 2023; 14: 2266.
9. Zhang C, Zhang L, Wu W, Gao F, Li RQ, Song W, et al. Artificial super neutrophils for inflammation targeting and hclo generation against tumors and infections. *Adv Mater*. 2019; 31: e1901179.
10. Oroojalian F, Beygi M, Baradaran B, Mokhtarzadeh A, Shahbazi MA. Immune cell membrane-coated biomimetic nanoparticles for targeted cancer therapy. *Small*. 2021; 17: e2006484.
11. Cui C, Chakraborty K, Tang XA, Zhou G, Schoenfelt KQ, Becker KM, et al. Neutrophil elastase selectively kills cancer cells and attenuates tumorigenesis. *Cell*. 2021; 184: 3163–77.e21.

- 763 12. Cui T, Zhang Y, Qin G, Wei Y, Yang J, Huang Y, et al. A neutrophil mimicking
764 metal-porphyrin-based nanodevice loaded with porcine pancreatic elastase for cancer therapy. *Nat*
765 *Commun.* 2023; 14: 1974.
- 766 13. Senior RM, Bielefeld DR, Starcher BC. Comparison of the elastolytic effects of human leukocyte
767 elastase and porcine pancreatic elastase. *Adv Exp Med Biol.* 1977; 79: 249–61.
- 768 14. Morrison HM, Kramps JA, Burnett D, Stockley RA. Lung lavage fluid from patients with alpha
769 1-proteinase inhibitor deficiency or chronic obstructive bronchitis: anti-elastase function and cell profile.
770 *Clin Sci (Lond).* 1987; 72: 373–81.
- 771 15. Li JJ, Mcadam KP. Human amyloid P component: an elastase inhibitor. *Scand J Immunol.* 1984; 20:
772 219–26.
- 773 16. Kinoshita T, Kitatani T, Warizaya M, Tada T. Structure of the complex of porcine pancreatic
774 elastase with a trimacrocytic peptide inhibitor FR901451. *Acta Crystallogr Sect F Struct Biol Cryst*
775 *Commun.* 2005; 61: 808–11.
- 776 17. Deng X, Chen K, Pang K, Liu X, Gao M, Ren J, et al. Key progresses of moe key laboratory of
777 macromolecular synthesis and functionalization in 2022. *Chin Chem Lett.* 2024; 35: 108861.
- 778 18. Wen Q, Cai Q, Fu P, Chang D, Xu X, Wen T, et al. Key progresses of moe key laboratory of
779 macromolecular synthesis and functionalization in 2021. *Chin Chem Lett.* 2023; 34: 107592.
- 780 19. Sadeghipour N, Davis SC, Tichauer KM. Generalized paired-agent kinetic model for in vivo
781 quantification of cancer cell-surface receptors under receptor saturation conditions. *Phys Med Biol.* 2017;
782 62: 394–414.
- 783 20. Parekh G, Shi Y, Zheng J, Zhang X, Leporatti S. Nano-carriers for targeted delivery and biomedical
784 imaging enhancement. *Ther Deliv.* 2018; 9: 451–68.
- 785 21. Gajbhiye KR, Gajbhiye V, Siddiqui IA, Gajbhiye JM. Crgd functionalized nanocarriers for targeted
786 delivery of bioactives. *J Drug Target.* 2019; 27: 111–24.
- 787 22. Wang C, Hu Q, Shen HM. Pharmacological inhibitors of autophagy as novel cancer therapeutic
788 agents. *Pharmacol Res.* 2016; 105: 164–75.
- 789 23. Heckmann BL, Yang X, Zhang X, Liu J. The autophagic inhibitor 3-methyladenine potently

stimulates PKA-dependent lipolysis in adipocytes. *Br J Pharmacol*. 2013; 168: 163–71.

24. Yang C, Ding Y, Mao Z, Wang W. Nanoplatform-mediated autophagy regulation and combined anti-tumor therapy for resistant tumors. *Int J Nanomedicine*. 2024; 19: 917–44.

25. Denny P, Feuermann M, Hill DP, Lovering RC, Plun-Favreau H, Roncaglia P. Exploring autophagy with gene ontology. *Autophagy*. 2018; 14: 419–36.

26. Chao X, Qian H, Wang S, Fulte S, Ding WX. Autophagy and liver cancer. *Clin Mol Hepatol*. 2020; 26: 606–17.

27. Moussay E, Kaoma T, Baginska J, Muller A, Van Moer K, Nicot N, et al. The acquisition of resistance to TNF α in breast cancer cells is associated with constitutive activation of autophagy as revealed by a transcriptome analysis using a custom microarray. *Autophagy*. 2011; 7: 760–70.

28. Pasquier B. Autophagy Inhibitors. *Cell Mol Life Sci*. 2016; 73: 985–1001.

29. Vishnupriya S, Priya Dharshini LC, Sakthivel KM, Rasmi RR. Autophagy markers as mediators of lung injury-implication for therapeutic intervention. *Life Sci*. 2020; 260: 118308.

30. Porter AG, Jänicke RU. Emerging roles of caspase-3 in apoptosis. *Cell Death Differ*. 1999; 6: 99–104.

31. Zamzami N, Marchetti P, Castedo M, Decaudin D, Macho A, Hirsch T, et al. Sequential reduction of mitochondrial transmembrane potential and generation of reactive oxygen species in early programmed cell death. *J Exp Med*. 1995; 182: 367–77.

32. Matés JM, Segura JA, Alonso FJ, Márquez J. Oxidative stress in apoptosis and cancer, an update. *Arch Toxicol*. 2012; 86: 1649–65.

33. Niu B, Liao K, Zhou Y, Wen T, Quan G, Pan X, et al. Application of glutathione depletion in cancer therapy: enhanced ROS-based therapy, ferroptosis, and chemotherapy. *Biomaterials*. 2021; 277: 121110.

34. Xue D, Zhou X, Qiu J. Emerging role of NRF2 in ROS-mediated tumor chemoresistance. *Biomed Pharmacother*. 2020; 131: 110676.

35. Lei J, Huo X, Duan W, Xu Q, Li R, Ma J, et al. α -Mangostin inhibits hypoxia-driven ROS-induced PSC activation and pancreatic cancer cell invasion. *Cancer Lett*. 2014; 347: 129–38.

36. Romero-Ramirez L, Cao H, Nelson D, Hammond E, Lee AH, Yoshida H, et al. Xbp1 is essential for

817 survival under hypoxic conditions and is required for tumor growth. *Cancer Res.* 2004; 64: 5943–7.

818 37. Poprac P, Jomova K, Simunkova M, Kollar V, Rhodes CJ, Valko M. Targeting free radicals in
819 oxidative stress-related human diseases. *Trends Pharmacol Sci.* 2017; 38: 592–607.

820 38. Zhong W, Guo F, Chen F, Law MK, Lu J, Shao D, et al. A multifunctional oxidative stress
821 nanoamplifier with ROS amplification and GSH exhaustion for enhanced chemodynamic therapy. *Front*
822 *Pharmacol.* 2022; 13: 1044083.

823 39. Sohrabi F, Dianat M, Badavi M, Radan M, Mard SA. Gallic acid suppresses inflammation and
824 oxidative stress through modulating Nrf2-HO-1-NF- κ B signaling pathways in elastase-induced
825 emphysema in rats. *Environ Sci Pollut Res Int.* 2021; 28: 56822–34.

826 40. Liu Z, Nan P, Gong Y, Tian L, Zheng Y, Wu Z. Endoplasmic reticulum stress-triggered ferroptosis
827 via the XBP1-Hrd1-Nrf2 pathway induces EMT progression in diabetic nephropathy. *Biomed*
828 *Pharmacother.* 2023; 164: 114897.

829 41. Hayes JD, Dinkova-Kostova AT, Tew KD. Oxidative stress in cancer. *Cancer Cell.* 2020; 38:
830 167–97.

831 42. Zhuang J, Nie G, Hu R, Wang C, Xing C, Li G, et al. Inhibition of autophagy aggravates
832 molybdenum-induced mitochondrial dysfunction by aggravating oxidative stress in duck renal tubular
833 epithelial cells. *Ecotoxicol Environ Saf.* 2021; 209: 111771.

834 43. Hou Y, Wang J, Feng J. The neuroprotective effects of curcumin are associated with the regulation
835 of the reciprocal function between autophagy and HIF-1 α in cerebral ischemia-reperfusion injury. *Drug*
836 *Des Devel Ther.* 2019; 13: 1135–44.

837 44. Shin D, Kim EH, Lee J, Roh JL. Rita plus 3-MA overcomes chemoresistance of head and neck
838 cancer cells via dual inhibition of autophagy and antioxidant systems. *Redox Biol.* 2017; 13: 219–27.

839 45. Li J, Ni M, Lee B, Barron E, Hinton DR, Lee AS. The unfolded protein response regulator
840 GRP78/BiP is required for endoplasmic reticulum integrity and stress-induced autophagy in mammalian
841 cells. *Cell Death Differ.* 2008; 15: 1460–71.

842 46. Nagao M, Nakajima Y, Hisanaga M, Kayagaki N, Kanehiro H, Aomatsu Y, et al. The alteration of
843 Fas receptor and ligand system in hepatocellular carcinomas: how do hepatoma cells escape from the

844 host immune surveillance in vivo. *Hepatology*. 1999; 30: 413–21.

845 47. Mooli RGR, Mukhi D, Ramakrishnan SK. Oxidative stress and redox signaling in the
846 pathophysiology of liver diseases. *Compr Physiol*. 2022; 12: 3167–92.

847 48. Hino K, Yanatori I, Hara Y, Nishina S. Iron and liver cancer: an inseparable connection. *Febs J*.
848 2022; 289: 7810–29.

849 49. Houghton AM, Rzymkiewicz DM, Ji H, Gregory AD, Egea EE, Metz HE, et al. Neutrophil
850 elastase-mediated degradation of IRS-1 accelerates lung tumor growth. *Nat Med*. 2010; 16: 219–23.

851 50. Liao W, Yang W, Shen Z, Ai W, Pan Q, Sun Y, et al. Heme oxygenase-1 regulates ferrous iron and
852 foxo1 in control of hepatic gluconeogenesis. *Diabetes*. 2021; 70: 696–709.

853 51. Gu X, Lai D, Liu S, Chen K, Zhang P, Chen B, et al. Hub genes, diagnostic model, and predicted
854 drugs related to iron metabolism in alzheimer's disease. *Front Aging Neurosci*. 2022; 14: 949083.

855 52. Kawabata H. Transferrin and transferrin receptors update. *Free Radic Biol Med*. 2019; 133: 46–54.

856 53. Nam H, Wang CY, Zhang L, Zhang W, Hojyo S, Fukada T, et al. ZIP14 and DMT1 in the liver,
857 pancreas, and heart are differentially regulated by iron deficiency and overload: implications for tissue
858 iron uptake in iron-related disorders. *Haematologica*. 2013; 98: 1049–57.

859 54. Muckenthaler MU, Rivella S, Hentze MW, Galy B. A red carpet for iron metabolism. *Cell*. 2017;
860 168: 344–61.

861 55. Sharp P, Tandy S, Yamaji S, Tennant J, Williams M, Singh Srani SK. Rapid regulation of divalent
862 metal transporter (DMT1) protein but not mRNA expression by non-haem iron in human intestinal
863 Caco-2 cells. *Febs Lett*. 2002; 510: 71–6.

864 56. Zhang Y, Hai Y, Miao Y, Qi X, Xue W, Luo Y, et al. The toxicity mechanism of different sized iron
865 nanoparticles on human breast cancer (MCF7) cells. *Food Chem*. 2021; 341: 128263.

866 57. Galaris D, Barbouti A, Pantopoulos K. Iron homeostasis and oxidative stress: an intimate
867 relationship. *Biochim Biophys Acta Mol Cell Res*. 2019; 1866: 118535.

868 58. Chen JL, Wu X, Yin D, Jia XH, Chen X, Gu ZY, et al. Autophagy inhibitors for cancer therapy:
869 small molecules and nanomedicines. *Pharmacol Ther*. 2023; 249: 108485.

870 59. Lu J, Gao X, Wang S, He Y, Ma X, Zhang T, et al. Advanced strategies to evade the mononuclear

phagocyte system clearance of nanomaterials. Exploration (Beijing). 2023; 3: 20220045.

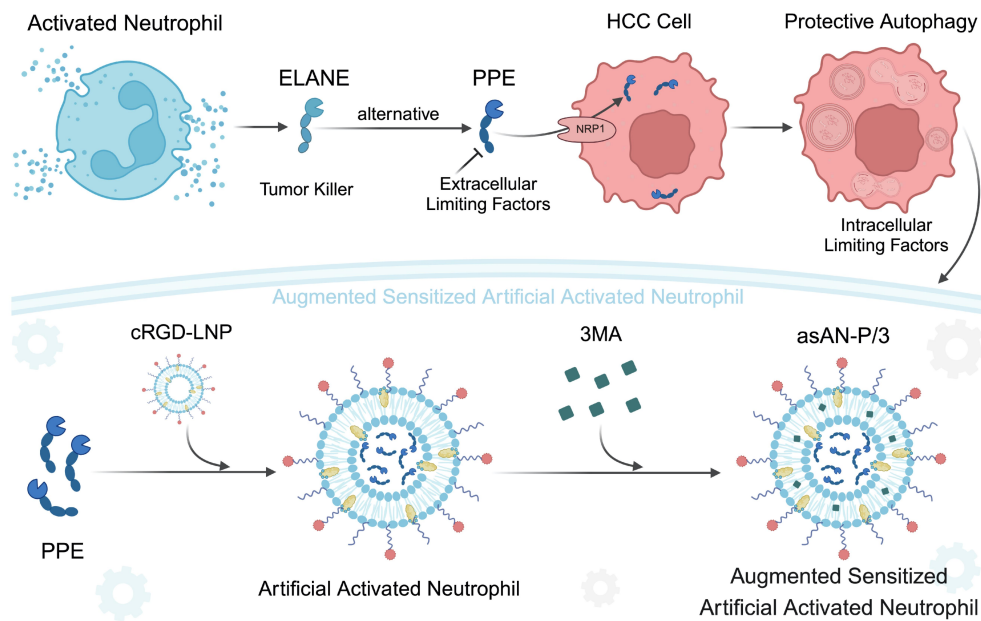
60. Graefe C, Eichhorn L, Wurst P, Kleiner J, Heine A, Panetas I, et al. Optimized Ki-67 staining in murine cells: a tool to determine cell proliferation. Mol Biol Rep. 2019; 46: 4631–43.

61. Darzynkiewicz Z, Galkowski D, Zhao H. Analysis of apoptosis by cytometry using tunel assay. Methods. 2008; 44: 250–4.

62. Liu Y, Zhang T, Zou X, Yuan Z, Li Y, Zang J, et al. Penumbra-targeted CircOGDH siRNA-loaded nanoparticles alleviate neuronal apoptosis in focal brain ischaemia. Stroke Vasc Neurol. 2024; 9: 134–44.

63. Xu X, Huang K, Dong F, Qumu S, Zhao Q, Niu H, et al. The heterogeneity of inflammatory response and emphysema in chronic obstructive pulmonary disease. Front Physiol. 2021; 12: 783396.

Figures



Scheme 1. Schematic illustration of the augmented sensitized artificial activated neutrophil asAN-P/3 designed for HCC therapy. ELANE served as the tumor killer in activated neutrophils, with selective cytotoxicity in cancer. PPE was a promising alternative of ELANE. However, protective

888 autophagy, receptors availability (intracellular), blood, extracellular connective tissue and non-target
889 (extracellular) limited PPE mediated therapeutic effectiveness against HCC. Based on the concept of the
890 artificial activated neutrophil, characterized by cRGD modified liposome loaded with PPE, 3-MA was
891 subsequently incorporated to sensitize the artificial activated neutrophil. Consequently, we developed an
892 augmented sensitized artificial activated neutrophil asAN-P/3 with stable targeting capability for HCC
893 therapy. cRGD-LNP: cRGD modified liposome; asAN-P/3: augmented sensitized artificial activated
894 neutrophil.

895

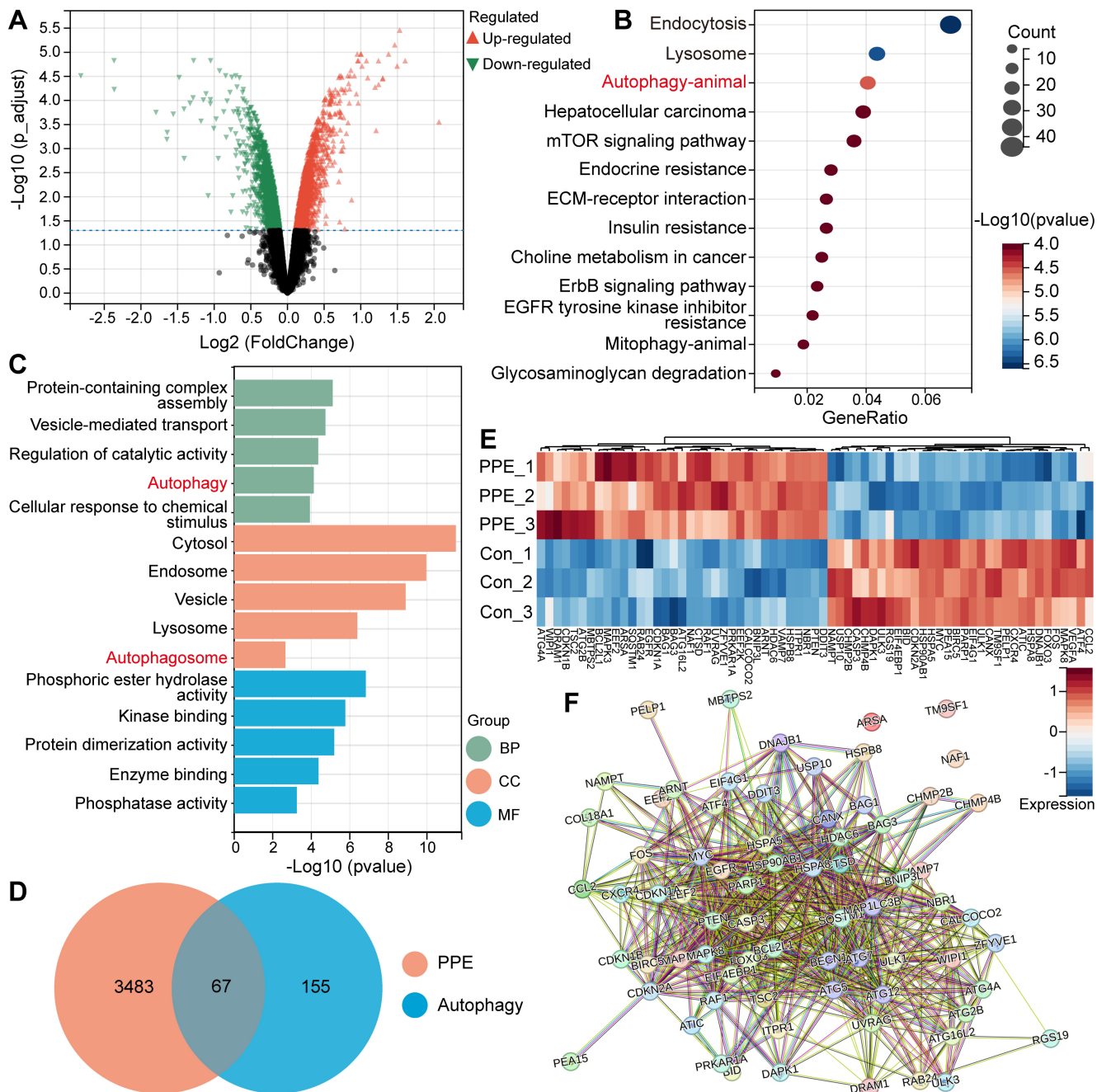
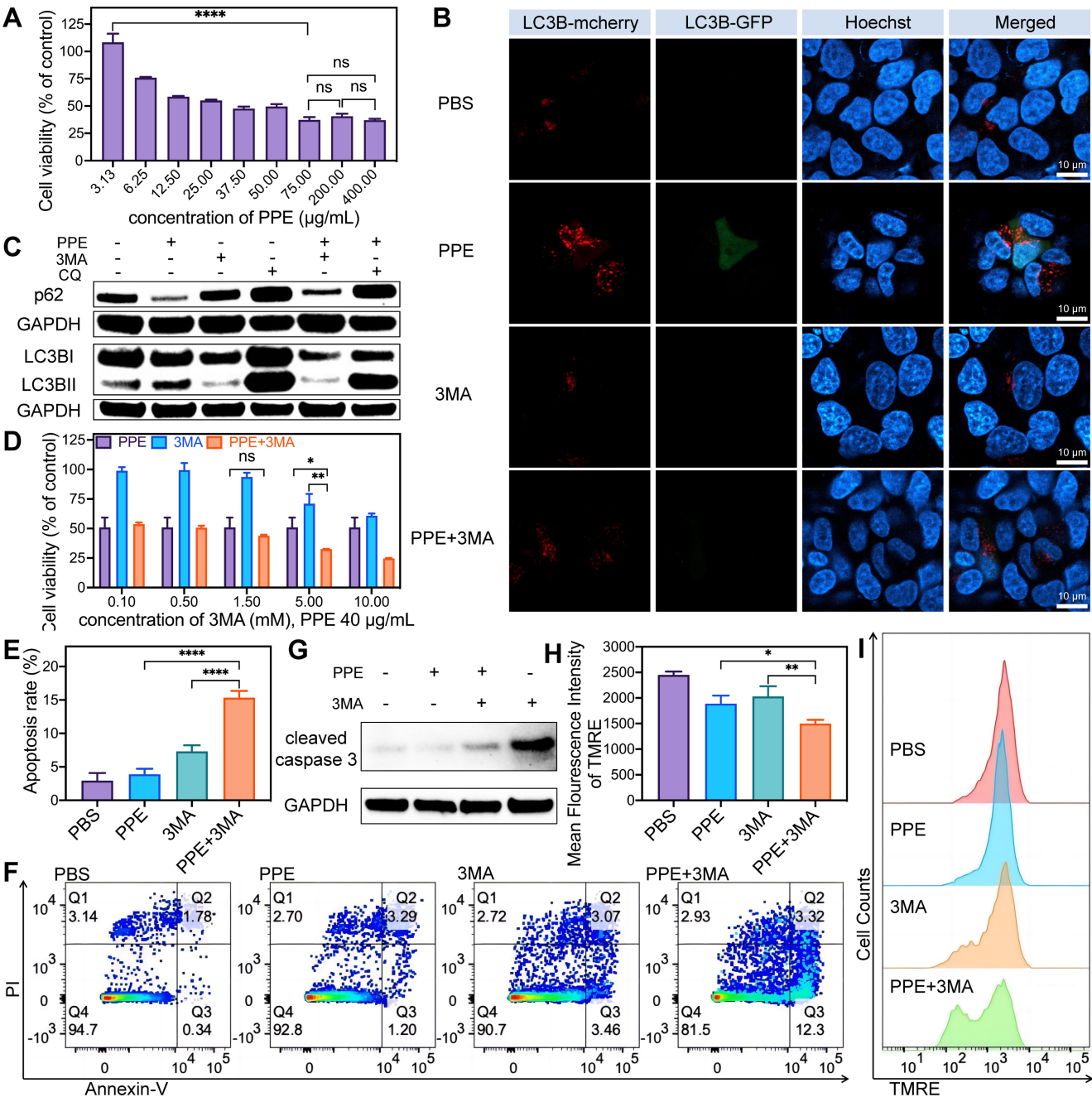


Figure 1. PPE activated protective autophagy in HCC. **A)** Volcano plot of differentially expressed genes in 3B cells treated with PPE compared to cells treated with PBS (control group). Red: up-regulated genes; Green: down-regulated genes. **B)** KEGG enrichment analysis of differentially up-regulated expressed genes in 3B cells treated with PPE compared to the control group (identified genes). **C)** GO enrichment analysis of the identified genes. BP: Biological Process; CC: Cellular Component; MF: Molecular Function. **D)** Venn plot in identification overlap differentially expressed

903 genes of 3B cells treated with PPE and autophagy related gene data series from Human Autophagy
 904 Database (HADb). E) Heat map of the 67 autophagy related differentially expressed genes between 3B
 905 cells treated with PPE and control group. Blue: low expression level; Red: high expression level. F) PPI
 906 network analysis of the 67 autophagy related differentially expressed genes of 3B cells treated with PPE.
 907



908
 909 **Figure 2. PPE in combination with autophagy inhibitor synergistically induced cell apoptosis in**

910 **HCC. A)** Cell viability of 3B cells after treatment with different concentration of PPE was quantified by
911 CCK8. **B)** Fluorescence images of LC3B expression on 3B cells after different treatments. Red
912 fluorescence from LC3B labeled with mcherry; green fluorescence from LC3B labeled with GFP; blue
913 fluorescence showed nucleus stained with Hoechst 33342. Scale bar is 10 μ m. **C)** Immunoblot analysis
914 of expression of autophagy related proteins p62, LC3B I and LC3B II of 3B cells after different
915 treatments. **D)** Cell viability of 3B cells after treatment with PPE (40 μ g/mL) and different concentration
916 of 3MA was quantified by CCK8. **E, F)** Apoptosis analysis of 3B cells after different treatments was
917 quantified by flow cytometry. **G)** Immunoblot analysis of expression of cell apoptosis related proteins
918 cleaved caspase 3 of 3B cells after different treatments. **H, I)** Mitochondrial membrane potential
919 analysis of 3B cells after different treatments was quantified by flow cytometry. Data were expressed as
920 mean \pm SD. * $p < 0.05$, ** $p < 0.01$, *** $p < 0.001$, **** $p < 0.0001$, ns: no statistical difference.

921

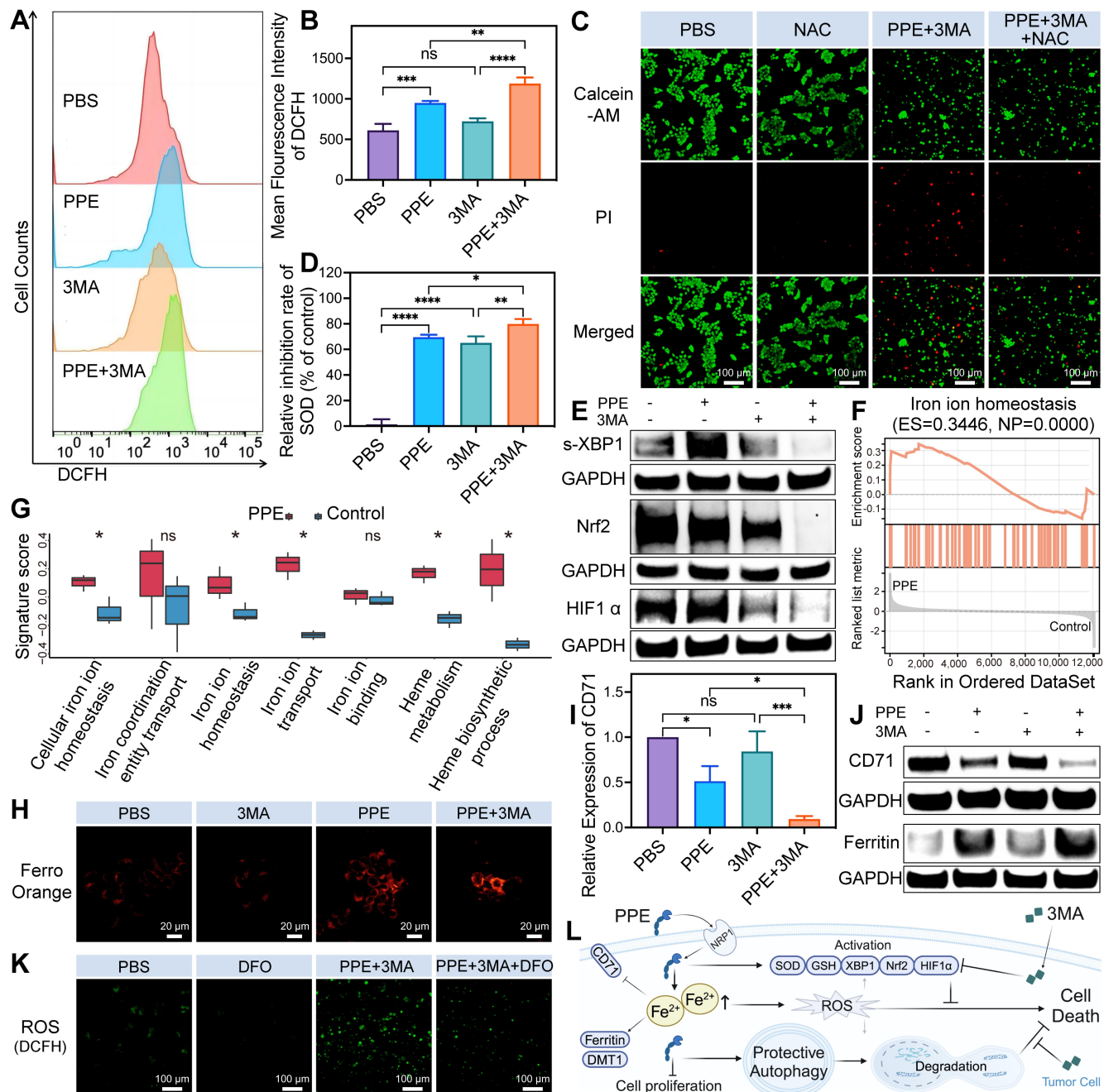


Figure 3. 3MA enhanced PPE mediated iron-related ROS-mediated cell apoptosis in HCC. A, B) ROS analysis of 3B cells after different treatments was quantified by flow cytometry. **C)** Cytotoxicity evaluation of 3B cells after different treatments was assessed by Calcein-AM/PI co-staining assay. Green fluorescence from Calcein-AM; red fluorescence from PI. Scale bar is 100 μ m. **D)** SOD inhibition rate evaluation of 3B cells after different treatments. **E)** Immunoblot analysis of expression of antioxidant nuclear transcription factors s-XBP1, Nrf2 and HIF1 α of 3B cells after different treatments.

929 **F)** Representative iron metabolism related pathway enriched in the identified genes was determined by
930 GSEA. **G)** Iron metabolism related pathways enriched in the identified genes were evaluated by GSVA
931 enrichment scores. **H)** Fluorescence images of ferrous ion on 3B cells after different treatments. Orange
932 fluorescence from FerroOrange. Scale bar is 20 μm . **I)** Expression of CD71 of 3B cells after different
933 treatments was quantified by immunoblot analysis. **J)** Immunoblot analysis of expression of iron
934 metabolism related proteins CD71, Ferritin of 3B cells after different treatments. **K)** Fluorescence
935 images of ROS on 3B cells after different treatments. Green fluorescence from DCFH. Scale bar is 100
936 μm . **L)** Schematic illustration of the functional mechanism of the enhanced therapeutic efficacy of PEE
937 by 3MA in HCC. Data were expressed as mean \pm SD. * $p < 0.05$, ** $p < 0.01$, *** $p < 0.001$, **** $p <$
938 0.0001, ns: no statistical difference.

939

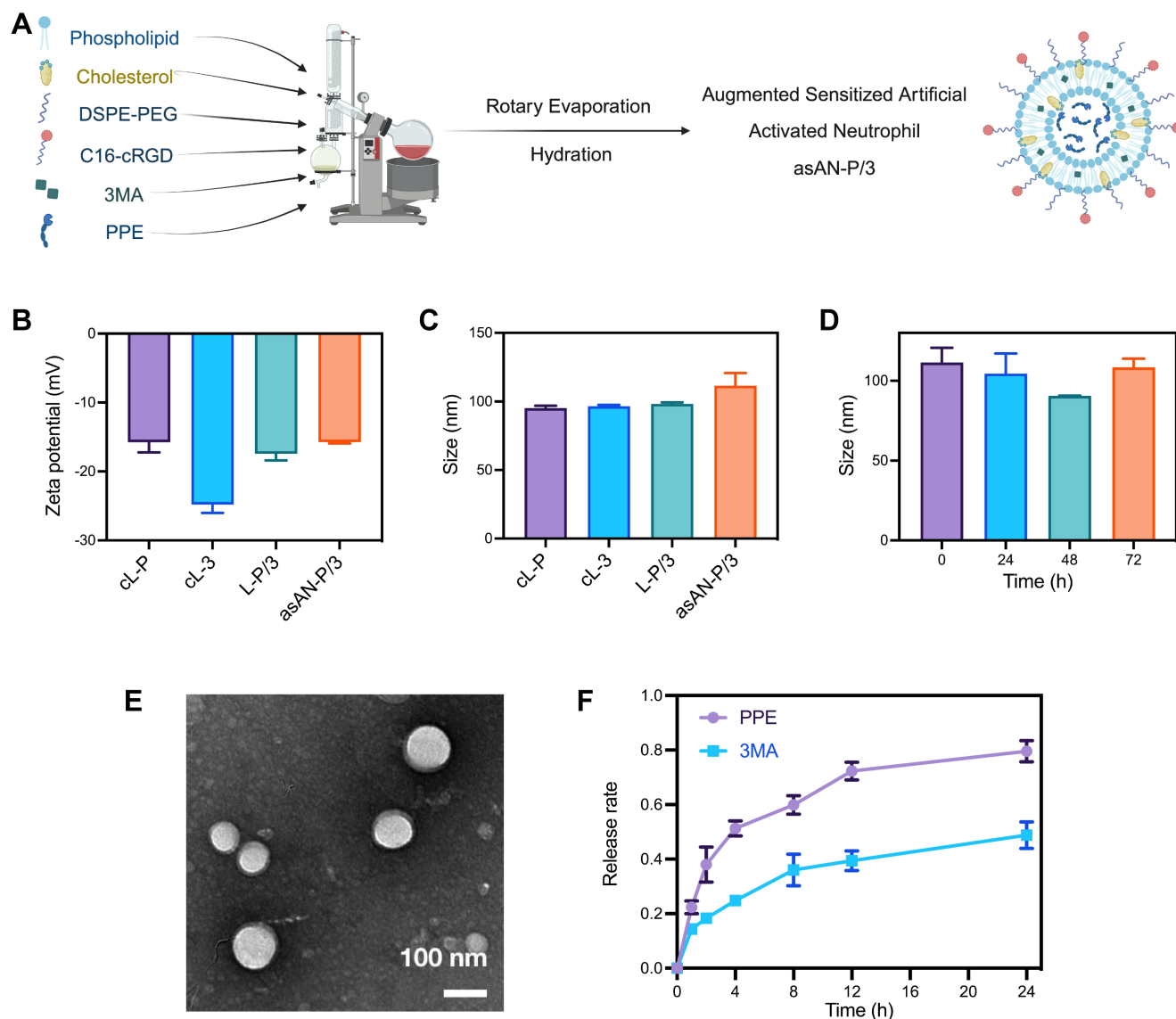
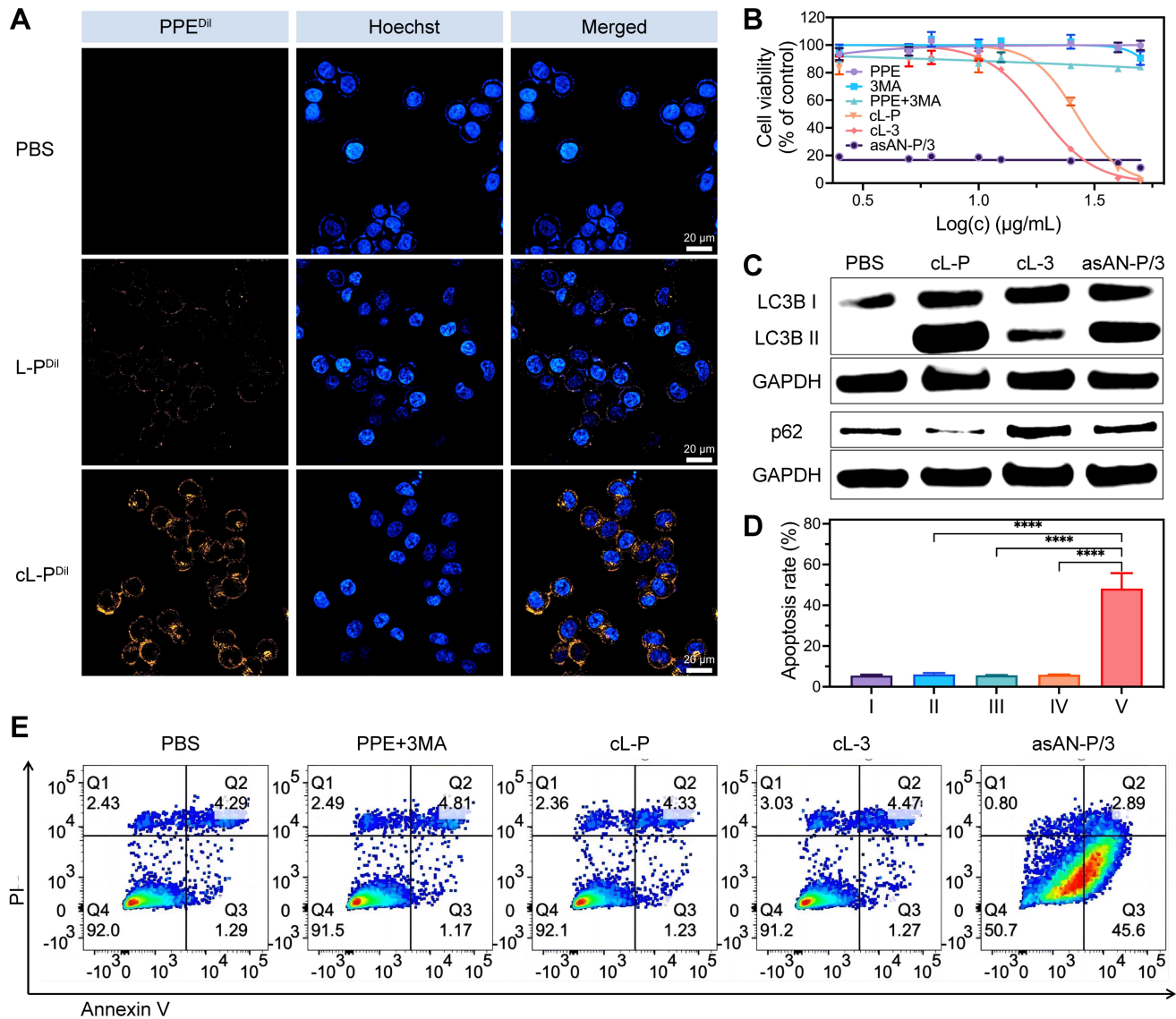


Figure 4. Preparation and characteristics of the augmented sensitized artificial activated neutrophil. **A)** The diagram of asAN-P/3 preparation by rotary evaporation method. **B)** The zeta potential of different nanomedicines. **C)** The size of different nanomedicines. **D)** The size of asAN-P/3 for different times. **E)** Transmission electron microscopy (TEM) images of asAN-P/3 in PBS. Scale bar is 100 nm. **F)** Release rate of different drugs loaded in the asAN-P/3 at different time points. Data were expressed as mean \pm SD.



I: PBS; II: PPE+3MA; III: cL-P; IV: cL-3; V: asAN-P/3

Figure 5. Enhanced targeting ability and therapeutic efficacy of the augmented sensitized artificial activated neutrophil *in vitro*. A) Confocal laser scanning microscopy (CLSM) images of 3B cells incubated with PBS, L-P or cL-P for 3 h. Orange fluorescence from PPE labeled with Dil; blue fluorescence showed nucleus stained with Hoechst 33342. Scale bar is 20 μm. B) Concentration dependent cytotoxicity evaluation of 3B cells after different treatments. The concentration of the nanomedicines depended on PPE, the concentration of 3MA was 3.67 times that of PPE. C) Immunoblot analysis of expression of autophagy related proteins LC3B I, LC3B II and p62 of 3B cells after different treatments. D, E) Apoptosis analysis of 3B cells after different treatments was quantified by flow

cytometry. I: PBS; II: PPE + 3MA; III: cL-P; IV: cL-3; V: asAN-P/3. L-P: liposome loaded with PPE; cL-P: cRGD modified liposome loaded with PPE; cL-P: cRGD modified liposome loaded with 3MA; asAN-P/3: augmented sensitized artificial activated neutrophil. Data were expressed as mean \pm SD. * p < 0.05, ** p < 0.01, *** p < 0.001, **** p < 0.0001.

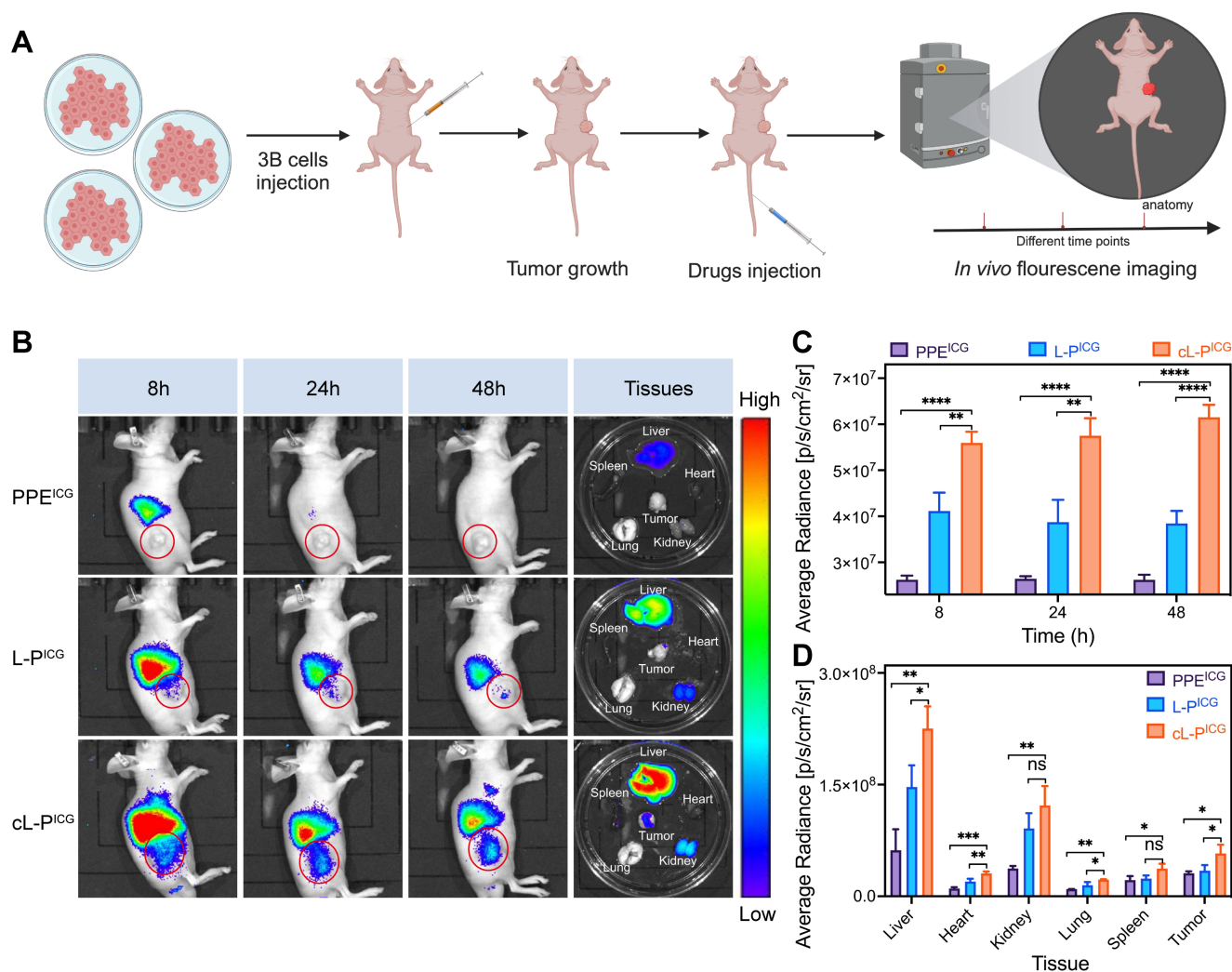
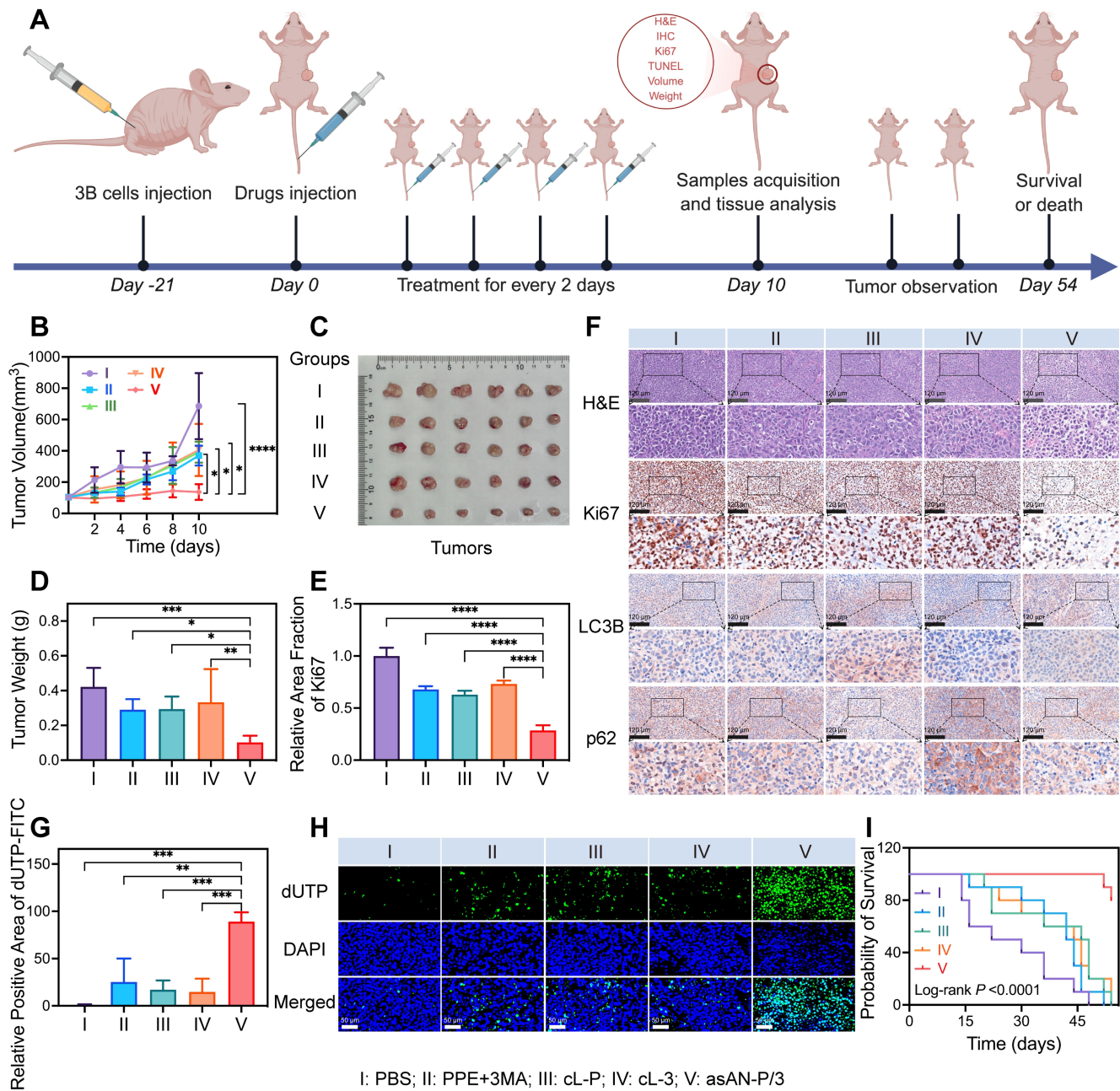


Figure 6. Enhanced tumor targeting ability of the augmented sensitized artificial activated neutrophil *in vivo*. A) Schematic illustration of the experiment design of *in vivo* fluorescence imaging of mice. B, C, D) *In vivo* targeting ability to tumor tissues of mice after injection of PPE^{ICG}, L-P^{ICG} or cL-P^{ICG}, at different time points was quantified by *in vivo* fluorescence imaging; and *ex vivo* accumulation in major organs and tumor tissues of mice was quantified by *ex vivo* fluorescence imaging. Red circle highlighted the tumor area. Data were expressed as mean \pm SD. * p < 0.05, ** p < 0.01, *** p < 0.001, **** p < 0.0001.

969 0.001, **** $p < 0.0001$, ns: no statistical difference.

970



971

972 **Figure 7. Enhanced therapeutic efficacy of the augmented sensitized artificial activated neutrophil**
973 **by regulating autophagy *in vivo*.** A) Schematic illustration of the experiment design of mice treatment
974 efficacy *in vivo*. B) Growth curve of tumors of mice after different treatments. C) Photograph of *ex vivo*
975 tumors from mice after different treatments on day 10. D) Tumor weight of *ex vivo* tumors from mice
976 after different treatments on day 10. E) Quantification of Ki67 immunohistochemistry analysis. F) H&E

977 staining, immunohistochemistry of Ki67, LC3B and p62 of tumors from mice after different treatments
978 on day 10. Scale bar is 120 μ m. **G)** Quantification of TUNEL apoptosis analysis. **H)** Fluorescence
979 images of TUNEL apoptosis analysis of tumors from mice after different treatments on day 10. Green
980 fluorescence from dUTP labeled with FITC; blue fluorescence from DAPI. Scale bar is 50 μ m. **I)**
981 Survival curve of mice after different treatments. I: **PBS**; II: **PPE + 3MA**; III: **cL-P**; IV: **cL-3**; V:
982 **asAN-P/3**. Data were expressed as mean \pm SD. * $p < 0.05$, ** $p < 0.01$, *** $p < 0.001$, **** $p < 0.0001$.

983

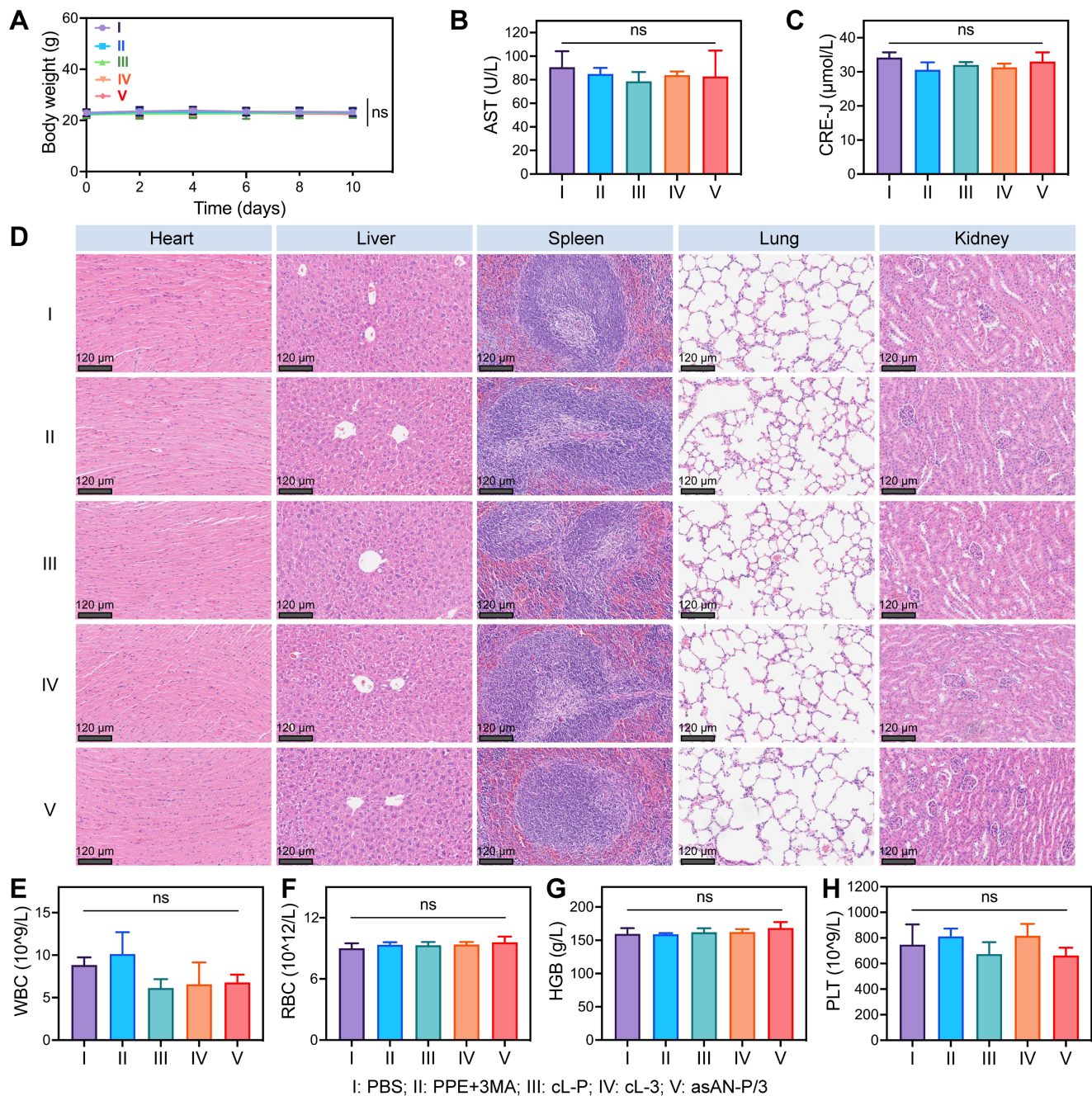
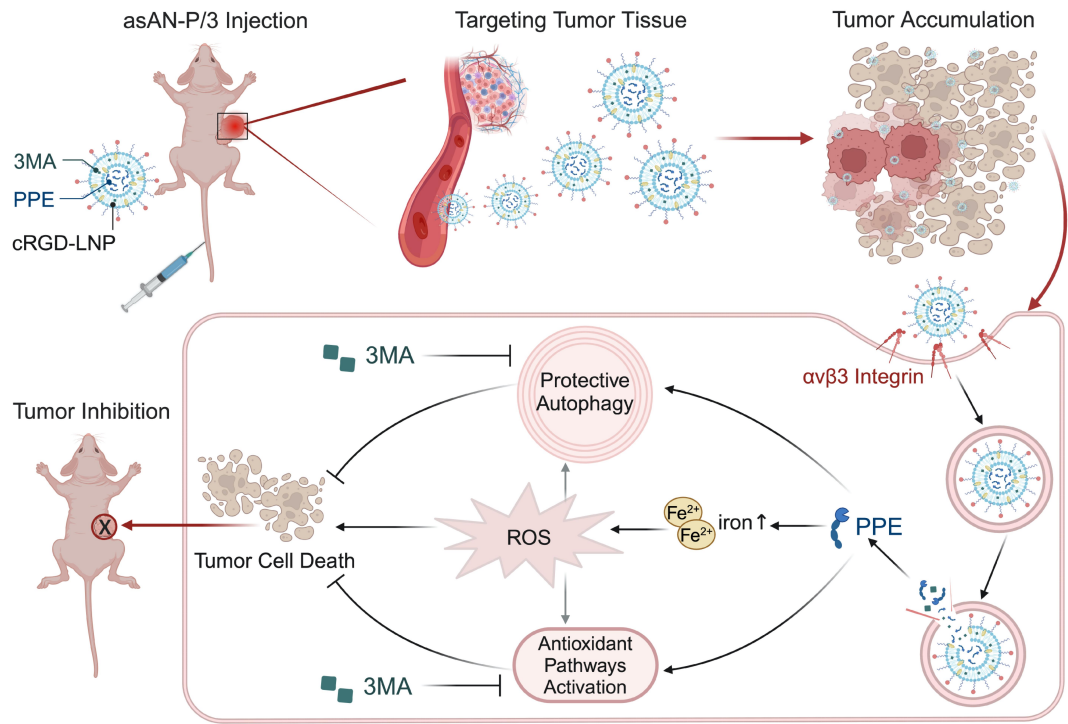


Figure 8. The bio-safety of the augmented sensitized artificial activated neutrophil *in vivo*. A) Curve of body weight of mice after different treatments at different time points. Hepatic and renal function were evaluated by the quantification of B) glutamic oxaloacetic transaminase (AST) and C) creatinine (CRE-J). D) H&E staining of major organs from mice after different treatments on day 10. Scale bar is 120 μm . E) Inflammatory state was evaluated by the quantification of white blood cell (WBC) from mice after different treatments on day 10. Hemolysis reaction was evaluated by

the quantification of **F**) red blood cell (RBC) and **G**) hemoglobin (HGB). **H**) Coagulation function was evaluated by the quantification of platelet (PLT) from mice after different treatments on day 10. I: **PBS**; II: **PPE + 3MA**; III: **cL-P**; IV: **cL-3**; V: **asAN-P/3**. Data were expressed as mean \pm SD. ns: no statistical difference.



Scheme 2. Schematic illustration of the augmented sensitized artificial activated neutrophil asAN-P/3 for HCC therapy. The alternative of neutrophil elastase, PPE, and the autophagy inhibitor 3MA were encapsulated in cRGD modified liposome to synthesize asAN-P/3, which were targeting transported by blood circulation and accumulated in tumor tissue. After entering the tumor cells through the interaction of cRGD with $\alpha v \beta 3$ integrin, PPE and 3MA were released. PPE destroyed the tumor cells by generating iron-dependent ROS, and 3MA inhibited both protective autophagy and antioxidant pathways, to sensitize PPE-mediated cell destruction and synergistically promote tumor cell death. This augmented sensitized artificial activated neutrophil significantly enhanced the targeting ability and therapeutic efficacy in HCC.